Infrasonic observations of the June 2009 Sarychev Peak eruption, Kuril Islands: implications for infrasonic monitoring of remote explosive volcanism

Robin S. Matoza, Alexis Le Pichon, Julien Vergoz, Pascal Herry, Jean-Marie Lalande
CEA/DAM/DIF, F-91297 Arpajon, France

Hee-il Lee, Il-Young Che
Earthquake Research Center, Korea Institute of Geoscience and Mineral Resources, Korea

Alexander Rybin
Sakhalin Volcanic Eruptions Response Team, *Institute of Marine Geology and Geophysics, Yuzhno-Sakhalinsk, Russia*

Author post-print of paper published in *Journal of Volcanology and Geothermal Research*

Matoza R.S., A. Le Pichon, J. Vergoz, P. Herry, J. Lalande, H. Lee, I. Che, and A. Rybin (2011), Infrasonic observations of the June 2009 Sarychev Peak eruption, Kuril Islands: Implications for infrasonic monitoring of remote explosive volcanism, *J. Volcanol. Geotherm. Res.*, **200**, 35-48, doi:10.1016/j.jvolgeores.2010.11.022

Abstract

Sarychev Peak (SP), located on Ostrov Matua, Kurils, erupted explosively during 11-16 June 2009. Whereas remote seismic stations did not record the eruption, we report atmospheric infrasound (acoustic wave ~0.01-20 Hz) observations of the eruption at seven infrasound arrays located at ranges of ~640-6,400 km from SP. The infrasound arrays consist of stations of the International Monitoring System global infrasound network and additional stations operated by the Korea Institute of Geoscience and Mineral Resources. Signals at the three closest recording stations IS44 (643 km, Petropavlovsk-Kamchatskiy, Kamchatka Krai, Russia), IS45 (1,690 km, Ussuriysk, Russia), and IS30 (1,774 km, Isumi, Japan) represent a detailed record of the explosion chronology that correlates well with an eruption chronology based on satellite data (TERRA, NOAA, MTSAT). The eruption chronology inferred from infrasound data has a higher temporal resolution than that obtained with satellite data. Atmosphere-corrected infrasonic source locations determined from backazimuth cross-bearings of first-arrivals have a mean centroid ~15 km from the true location of SP. Scatter in source locations of up to ~100 km result from currently unresolved details of atmospheric propagation and source complexity. We observe systematic time-variations in trace-velocity, backazimuth deviation, and signal frequency content at IS44. Preliminary investigation of atmospheric propagation from SP to IS44 indicates that these variations can be attributed to solar tide variability in the thermosphere. It is well known that additional information about active volcanic processes can be learned by deploying infrasonic sensors with seismometers at erupting volcanoes. This study further highlights the significant potential of infrasound arrays for monitoring volcanic regions such as the Kurils that have only sparse seismic network coverage.

1. Introduction

Sarychev Peak (SP), an andesitic stratovolcano (summit elevation 1446 m a.s.l.) on the northwest side of Ostrov Matua (Matua Island), Kurils (Figure 1), erupted explosively during 11-16 June 2009. The eruption was first indicated by satellite data acquired on 11 June 2009 that showed a thermal anomaly and weak ash emissions (SVERT, 2009). Subsequently, at ~22:16 UT 12 June 2009, spectacular photographs of an eruption column issuing from SP were taken by astronauts aboard the International Space Station (ISS) (Figure 1, inset). These photographs also captured ash dispersed at altitude from previous eruptions, and pyroclastic flows in the process of descending the mountain (Figure 1, inset). Due to the remote location of the Kurils, ground-based observations are sparse. In particular, no seismic network was in place on SP at the time of the eruption and the eruption did not register on any remote seismic stations (e.g., seismic stations on Paramushir, Iturup and Sakhalin at distances of 352 km, 512 km and 800 km from SP, respectively). Therefore, there are no seismic data connected with this event. Consequently, previous to the current study, the chronology of the eruption has been constructed primarily with satellite data (TERRA, NOAA, MTSAT; SVERT, 2009). Although the Kurils are sparsely populated, they are located within a heavily travelled air corridor linking Europe, North America, and northern Asia. Effective monitoring of Kuril volcanism is therefore imperative for aviation safety (Neal et al., 2009).

Acoustic waves with frequencies ~0.01-20 Hz are named *infrasound*. Here we report atmospheric infrasound observations of the June 2009 SP eruption. Energetic vulcanian and plinian explosions can radiate large-amplitude infrasound directly into the atmosphere (e.g., Garces et al., 2008; Matoza et al., 2009; Fee et al., 2010a, 2010b). In contrast, seismicity (eruption tremor) recorded on dedicated volcano-seismic networks during vulcanian and plinian explosions may result from subsurface processes and/or limited air-ground acoustic-seismic coupling (Matoza, 2009). Consequently, large-amplitude infrasound signals may delineate the exact timing of volcanic explosions, whereas eruption seismicity may be relatively weak or not necessarily correlated with the timing of eruption into the atmosphere.

Infrasound can propagate over large distances in the atmosphere due to low attenuation (Sutherland and Bass, 2004) and due to the formation of waveguides by temperature

and wind variations with altitude (e.g., Garces et al., 1998). Whereas remote seismic stations did not record the SP eruption, we report infrasound signals propagating as far as 6,433 km from SP in the stratospheric waveguide. However, the details of infrasound propagation in the atmosphere remain a subject of active research (Le Pichon et al., 2010a). For atmospheric studies, volcanoes can represent repetitive sources of infrasound from known and fixed source locations, making them essential ground-truth sources for assessing models of infrasound propagation and atmospheric specifications (Le Pichon et al., 2005). The explosive phase of the eruption sequence at SP lasted for 5-6 days in duration. We use array processing to estimate infrasound wavefront parameters, e.g., backazimuth and trace-velocity (apparent velocity of the wavefront across the array), as a function of time during the eruption sequence. We show that the estimated backazimuth, trace-velocity and signal frequency content of infrasonic signals from repetitive explosions exhibit systematic variations with time that can be explained by atmospheric variability.

This paper is organized as follows. In section 2 we describe the sequence of observations at seven infrasound arrays deployed at ranges of ~640-6,400 km from SP. We show how these infrasound observations permit the reconstruction of a more detailed eruption chronology (i.e., with a higher temporal resolution) than is possible with satellite data alone. We then highlight some observed signal characteristics resulting from atmospheric propagation and illustrate the effects of atmospheric propagation on infrasound source locations. In section 3, we model the infrasound propagation using 3D ray-tracing and realistic atmospheric specifications and attempt a source location including atmospheric corrections. We then illustrate with parabolic equation modeling how diffraction and scattering may influence infrasonic propagation from explosive volcanic eruptions. Sections 4 and 5 consist of discussion and conclusions.

2. Observations

2.1. Data

The International Monitoring System (IMS) includes a global network of infrasonic stations designed to detect atmospheric explosions anywhere on the planet (Christie and Campus, 2010). Each infrasound station consists of an array of at least 4 infrasonic sensors with a flat response typically from 0.01 to 8 Hz (sampled at 20 Hz) and a

sensitivity of about 0.1 mPa per count. Figure 1 shows the IMS infrasound stations and an additional station, YAG, operated by the Korea Institute of Geoscience and Mineral Resources (KIGAM), used in this study. Signals from SP were also recorded at other KIGAM infrasound stations, however, we selected one station (YAG) for use in this study since the KIGAM stations fall at similar ranges from SP. IS44 (Kamchatka) is the closest station to SP at a range of 643 km.

Figure 2 shows the results of applying Progressive MultiChannel Correlation (PMCC) array processing (Cansi, 1995; Le Pichon et al., 2010b) to the infrasound stations labeled in Figure 1. PMCC estimates wavefront properties of coherent acoustic energy as a function of time at an array by considering correlation time-delays between successive array element triplets (Cansi, 1995). A grid search is performed over successive time windows and frequency bands. A coherent arrival in a particular time window and frequency band is registered as a "pixel". Pixels are then grouped into "families" of pixels sharing common wavefront properties. PMCC processing was performed in 15 log-spaced frequency bands between 0.02 and 9.5 Hz (window length varied from 120 s to 30 s with overlaps 90 % of window length). Figure 2 shows all PMCC pixels coming from an azimuth corresponding to SP +/-15° as viewed from each array (i.e., for each station, we show all PMCC detections that have an azimuth +/-15° of the azimuth of the great-circle path from the station to SP). In order to align the detections in time and facilitate association of the recordings at the various stations, we have applied a time shift to the detections at each array in Figure 2. The time shift corresponds to the range divided by a constant celerity of 0.33 km/s. Celerity is defined as the total range travelled divided by the propagation time. The celerity of 0.33 km/s used in Figure 2 is typically appropriate for infrasound propagating in the troposphere. For infrasonic propagation in the stratosphere, a slower celerity of 0.3 km/s is more appropriate. Thus, tropospheric arrivals from SP align vertically on Figure 2, whereas stratospheric arrivals will not align perfectly in the vertical. This is barely visible for the time-scale of data shown in Figure 2.

Figure 2 shows that a long sequence of infrasonic signals arrived from the direction of SP at IS44, IS45, IS30, and YAG between Julian days 162-167 2009 (11-16 June 2009). In addition, several of the signals with larger amplitude propagated to longer range. IS31 (Kazakhstan) is the furthest recording station at a range of 6,433 km. We note that IS53,

IS39, and IS59 did not record infrasound from SP despite being closer to the source than IS31 (Figure 2). The pattern of signal detectability on Figure 1 is consistent with propagation of the signals to long range in the seasonal stratospheric duct. Stratospheric winds blow westward (from east to west) in the summer at midlatitudes, leading to favorable signal reception to the west of a source. IS53, IS59, and IS39 are located to the east and south of SP where stratospheric propagation is not generally predicted at this time of year at these latitudes. It is known that ~80 % of all infrasonic signals in the 0.2-2 Hz band recorded globally on the IMS network correspond to signals received in the stratospheric downwind direction (Le Pichon et al., 2009).

We note in Figure 2 the presence of some coherent noise sources falling within the chosen azimuth bounds, but that are not likely to be signal from SP. This coherent noise is not associated across multiple stations. In particular, continuous coherent signal is recorded at backazimuths greater than the true backazimuth of SP at IS30 and YAG. This signal is likely microbarom noise (e.g., Willis et al., 2004) given its continuous nature, frequency content (not shown on Figure 2), and direction pointing towards the ocean (approximately same direction as SP for these stations located near eastern coastlines).

2.2. Observed signal chronology at IS44

IS44 is the closest station to SP and recorded the greatest number of detections associated with the eruption. The chronology of signals recorded at this array therefore gives the best indication available of the chronology of the SP eruption sequence. We note in Figure 2 that all detections observed at IS45 and IS30 are also observed at IS44 but not vice versa. Figure 3 shows the infrasonic waveforms at IS44. The waveforms correspond to a time-domain beam (e.g., DeFatta et al., 1988) at the great-circle azimuth of SP and a trace-velocity of 0.34 km/s (typical trace-velocity for first-arrivals and majority of detections at IS44, see section 2.3). The waveforms in Figure 3 are shown at their true observed time and are not corrected by celerity back to an assumed origin time at SP. At the beginning of the sequence there are three impulsive signals between 6 am and 9 am UT on 11 June 2009 (day 162). These signals appear to represent earlier, less-vigorous explosion precursors to the main phase. Following these explosions there is a repose in observed signal for ~17 hours. Then, beginning at ~02:10:44 UT 12 June 2009 (day 163), there is a long sequence of energetic coherent infrasonic signal

originating from SP (Figure 2). For the first ~10 hours following 02:10:44 UT 12 June 2009, the signal is a convoluted superposition of broadband infrasonic tremor and more impulsive explosion signals, typical of vulcanian-plinian eruptions (Matoza et al., 2009; Fee et al., 2010b). This then transitions gradually into a series of more isolated explosion signals by ~12:00 UT 12 June 2009. Fifteen such repetitive explosions occur between 12:00 and 24:00 UT on 12 June 2009 with the inter-event time spacing gradually increasing during this time (indicated by arrows between the mid-point and the end of the second trace on Figure 3). From the beginning of 13 June 2009 (day 164) to the end of 15 June 2009 (day 166) we count ten large explosions originating from SP. These signals consist of broadband, high-amplitude infrasonic tremor signals lasting tens of minutes to over an hour in duration each. The amplitude of these explosion signals are generally of the same amplitude or larger than the sequence recorded on 12 June (day 163). Consequently, these signals were recorded further from the source (Figure 2). The explosion on Figure 3 between 17:00 and 18:00 UT on 15 June (day 166) was recorded at IS31 (Figure 2). The waveforms in Figure 3 are further complicated by local wind noise and a regional seismic event (traveling at seismic velocity, azimuth not associated to SP). The level of detail visible in the waveforms at IS44 at a range of 643 km is remarkable and points to the utility of remote infrasonic arrays for monitoring erupting volcanoes.

The signal chronology can be analyzed in more detail by considering the rate of PMCC detections as a function of time. A waveform plot such as Figure 3 shows clearly those signals that have high signal-to-noise ratio, but no distinction is made between coherent acoustic signal and incoherent noise (e.g., wind noise). In addition, it is difficult in Figure 3 to identify signal packet durations for individual arrivals within the ~10 hour, highly convoluted sequence at the onset of the main phase between ~02:10:44 UT and 12:00 UT on 12 June 2009 (day 163). Figure 4 shows a bar graph of the number of PMCC detections at IS44 occurring per minute from an azimuth +/-15° of SP. Since these detections only correspond to coherent signal originating from SP, it is easier in Figure 4 than in Figure 3 to separate the individual signal arrivals. From this information we pick automatically the onset time t_{on} and end-time t_{off} of the signal packets with an accuracy of 1 minute. Table 1 shows the list of signals identified with this method. The signal onset times have also been corrected back to the origin time at SP assuming a celerity of

0.33 km/s. Considering that the true celerity for first arrivals may vary between 0.30 and 0.34 km/s we estimate that the origin times at SP listed in Table 1 would be accurate to ~5 minutes. Following the identification of t_{on} and t_{off} for all signals in the sequence, we applied a final procedure to identify the average dominant period (sec) and amplitude (Pa) of each signal received from SP. The raw data for IS44 were beamformed sequentially at the azimuth and trace-velocity of each PMCC family and the dominant period and amplitude of the signal packets were extracted into Table 1.

In Figure 4 we summarize the information in Table 1 and the results of our procedure by depicting the durations of coherent signal by black horizontal bars. This information is then directly compared to the explosion chronology (grey bars) inferred from satellite data by the Sakhalin Volcanic Eruptions Response Team (SVERT) (Table 2). SVERT creates daily information reports of volcanic activity in the Kurils using data primarily from high-orbital meteorological satellites TERRA (spectroradiometer MODIS) and NOAA (spectroradiometer AVHRR). The satellite data have an approximate temporal resolution of +/-15 minutes during the eruption sequence. The grey bars in Figure 4 are centered on the origin times of explosions inferred by SVERT. The horizontal extent of the grey bars is 30 minutes, to represent the estimated +/-15 minutes temporal resolution of the satellite method. The vertical extent of the grey bars is scaled relative to the maximum altitude of each explosion plume inferred by SVERT. The explosion at ~2130 UT Julian day 164 has the maximum altitude of 21 km inferred by SVERT (Table 2). Other plumes have inferred altitudes ranging typically from 5 to 10 km (Table 2). In general, we note that the correlation between the explosion origin times inferred by infrasound data (black bars) and those inferred by satellite data (grey bars) are in good agreement (Figure 4). Almost every explosion identified by SVERT has a significant associated infrasonic detection at IS44. We note, however, that it appears we are able with infrasound data to construct the eruption chronology with greater temporal resolution than is possible with satellite data alone. In particular, for the time period between Julian days 163-164.5 2009 (Figure 4, upper panel) there are many more individual infrasonic detection packets observed than there are explosions inferred by satellite data. The timing of these infrasonic detection packets may be inferred as a detailed record of the explosion activity at SP. We note that it is possible that not every explosion was recorded at IS44. Due to signal detectability and propagation effects,

explosions occurring with smaller amplitude may not have been recorded above noise at IS44.

2.3. Infrasonic phase identification and signal variability

To a first order, infrasonic propagation in the atmosphere is governed by vertical gradients in the temperature and horizontal winds. Propagation of infrasonic signals in the atmosphere can be considered loosely to take place in three main ducts formed by: 1) the troposphere (~0-10 km), 2) the stratosphere (~10-50 km), and 3) the thermosphere (> 90 km) (Brown et al., 2002; Drob et al., 2003). Each of these idealized infrasonic "phases" (tropospheric phase *Iw*, stratospheric phase *Is*, and thermospheric phase *It*) are predicted to arrive at an infrasound array with a different value of trace-velocity, backazimuth deviation, frequency content and celerity. Trace-velocity v_t is related to the angle of incidence α of arrivals at an array by $\alpha = \cos^{-1}(c / v_t)$, where $c = \sqrt{\frac{\gamma RT}{M}}$, the sound speed as a function of temperature *T*, with γ the ratio of specific heats, *R* the molar gas constant, and *M* the molar mass of air. For instance, *Iw* have lower trace-velocities and higher celerities (energy propagates almost horizontally along the ground), while *It* have higher trace-velocities and lower celerities. Differences in backazimuth deviation result from variable exposure to cross-winds encountered along different propagation paths. However, since the vertical temperature and wind structure of the atmosphere is temporally and spatially dependent, and since significant scattering (Kulichkov, 2010) and diffraction (Bass, 1991) can occur during infrasound propagation, the classification of observed infrasonic signals into these three idealized phases can be difficult in practice (Brown et al., 2002).

Furthermore, the observed signals from SP are complicated by the long durations of the acoustic source-time functions. Sustained vulcanian and plinian volcanic eruptions generate sustained, broadband acoustic source functions which can last from tens of minutes to hours in duration (Matoza et al., 2009). The observed high-amplitude signals with durations of tens of minutes to hours are consistent with such a sustained volcano-acoustic source (Figure 3). When convolved with an atmospheric propagation response, the result is a complicated wavetrain recorded at an array. For instance, for the range of IS44 (~643 km), the time difference between an *Iw* travelling with celerity 0.33 km/s

and an *It* travelling with celerity 0.25 km/s would be ~10 minutes. In contrast, typical signal durations observed at IS44 are ~20 minutes. Therefore, energy traveling in the troposphere, stratosphere, and thermosphere may all arrive at an array simultaneously from a long-duration volcanic source. Scattering could lead to further mixing of infrasonic phases (Kulichkov, 2010).

Figure 5 shows details of the PMCC-derived signal properties at IS44, IS45, and IS30 during Julian days 163-164.5 2009 (UTC). During 163.5-164, the range of observed trace-velocities and backazimuths at IS44 gradually expands and then decreases. At ~163.5 only a limited range of azimuth and trace-velocity values are observed for signals at IS44, while by ~163.75, a larger range of azimuths and trace-velocities are observed. The increase in the range of observed azimuths and trace-velocities between 163.5 and 163.75 can be explained by an increase in the variety of infrasonic phases being detected. Figure 6 shows more details of the detections at IS44 and IS45 during Julian days 163.5-164. During this time at IS44, each volcanic signal of duration ~20 min consists of a continuous sweep from low to high trace-velocity (Figure 6a), from high to low dominant frequency (Figure 6b), and from low to high azimuth deviation (Figure 6c). These gradually evolving signal properties may be explained by mixed infrasonic phases arriving at the array from a sustained source-time function. In particular, the observations are broadly consistent with a gradual transition from dominantly tropospheric, through dominantly stratospheric, to dominantly thermospheric trajectories. It would be difficult to separate this continuous sweep of detections into individual tropospheric, stratospheric and thermospheric components. We note that plots of observed backazimuth vs. trace-velocity (or vs. frequency) do not help with phase discrimination because the detections to not cluster into distinct groups. In section 3, we perform preliminary simulations aimed at explaining some of the observed signal features at IS44.

In contrast, at IS45 (Figure 6d-f), the volcanic signals typically consist of a sweep lasting ~15 minutes from high to low trace-velocity, from high to low azimuth deviation, with frequency content remaining relatively constant. In some cases, two distinct arrivals can be observed in trace-velocity (e.g., at ~163.8, Figure 6d). This arrival sequence at IS45 is somewhat unusual. It is not typical to observe a transition from high to low trace-

velocity. However, such arrival sequences may be explained by unusual propagation scenarios (Kulichkov et al., 2004; Evers and Haak, 2007). Kulichkov et al., (2004) and Evers and Haak, (2007) showed that acoustic energy analogous to seismic head waves may propagate at high-celerity at high-elevation (in the stratosphere) for an extended time before propagating back to the ground. These so-called infrasonic "forerunners" may explain the initial arrivals at IS45 with high trace-velocity and fast celerities (Evers and Haak, 2007). We note, however, that the range of 1690 km from SP to IS45 is larger than the ranges of ~640 km and ~510 km considered by Kulichkov et al., (2004) and Evers and Haak, (2007) respectively. Hence, further work (beyond the scope of the present study) is required to understand in better detail the propagation from SP to IS45.

2.4. Source location by cross-bearings with no atmospheric correction

Here we attempt an infrasound source location using backazimuth cross-bearings from the three closest stations: IS44, IS45 and IS30 (Figure 7a). At this stage, we do not correct the observed backazimuth values for deflection induced by atmospheric propagation. This illustrates the expected error in source location induced by atmospheric propagation effects (Evers and Haak, 2005). The problem of infrasonic source location is complicated by the overlapping nature of the observed infrasonic phases (section 2.3). Infrasound source location is usually performed on selected infrasonic phases (e.g., Ceranna et al., 2009). Since phase discrimination is challenging (section 2.3), here we attempt source locations based on 1) a running median of all observed backazimuth values and 2) the median backazimuth of first-arrivals in each coherent detection packet. For (1), the median backazimuth is calculated from all detections in a 15-minute time window which is advanced in steps of 2 minutes. For (2), we take three 2-minute median values corresponding to the first 6 minutes of each coherent detection packet. The detections are then aligned in time by a chosen celerity (0.33 km/s in Figure 7) and any detections not occurring at the aligned time at all three infrasound stations are discarded. We note that we are using *a priori* knowledge of the source-receiver range to perform the alignment in time. For routine operational source location where the true source location is unknown, iterative variants of this method are required (Le Pichon et al., 2008). The results of this procedure are shown in Figure 7b (running median, 1 above) and Figure 7d (first-arrivals, 2 above). These observed

backazimuth values are used in the source location procedure. We note that during times of continuous infrasonic detection (e.g., Julian day ~163.25 to 163.5) the first-arrivals (Figure 7d) represent much fewer backazimuth values than the running median (Figure 7b).

The optimal source location is that which minimizes, in a least-squares sense, the difference in predicted and observed azimuth for all three stations (Le Pichon et al., 2008; Ceranna et al., 2009). Figures 7j and k show the source locations obtained. In Figures 7j and k we also show a 90 % confidence ellipse for source location assuming that azimuth standard deviations are 3° from true. An uncertainty of 3° is an upper bound for the uncertainty in backazimuth estimation using a typical IMS infrasound array configuration (Szuberla and Olson, 2004). The ellipse is estimated by repeating our source location procedure with 500 realizations consisting of the true great-circle backazimuths perturbed by Gaussian noise with a standard deviation of 3°. The ellipse illustrates the uncertainty in source location arising from the source-receiver geometry.

All source locations are offset to the northwest of SP (Figures 7j, 7k), consistent with deflection of the infrasound waves by the dominant east-west stratospheric winds. The mean source centroids are located at distances of ~33 km and ~39 km from the true location of SP when using a running median (Figure 7j) and first-arrivals (Figure 7k), respectively. We also observe significant scatter in the source locations resulting in source location errors sometimes exceeding 100 km (Figures 7c, 7e). A measure of the spread in source locations is given by the mean distance from each source location to the mean source centroid, which is ~25 km when using the running median and ~22 km for first-arrivals. This scatter is temporally dependent (Figures 7j, 7k).

Comparing Figures 7j and 7k illustrates the effects of the strong azimuth swings observed in the infrasonic detections (section 2.3) on source location estimates. These azimuth swings lead to rapid variations in the source location estimates (Figure 7j). As stated in section 2.3, the azimuth swings are likely a result of a gradual transition between *Iw*, *Is* and *It* arrivals, which are difficult to separate. However, the scatter is also aligned with the 3° 90 % confidence ellipse in the northeast-southwest direction, reflecting the limitations of the station geometry. We repeated our procedure, aligning

the detections in time using values of celerity ranging between 0.25 and 0.34 km/s without a significant change in the results. We also repeated our procedure with limited subsets of the detections corresponding to limited values of trace-velocity and frequency content corresponding to idealized values for *Iw*, *Is* and *It.* We again found that this did not have a significant effect on the source locations. We note that the scatter in source location estimates is not improved by treating first-arrivals (Figure 7k) vs. a running median of backazimuth values (Figure 7j). This points to the limitation of the source location procedure without considering detailed and accurate descriptions of the azimuth perturbations induced by atmospheric propagation. Reduction in the scatter shown in Figure 7j would require detailed predictions of the observed sweeps in azimuth in Figures 5 and 6. Figures 7f-7i and 7l-m correspond to a source re-location using an atmospheric correction described in section 3.1.

3. Propagation modeling

For an introduction to infrasound propagation in the atmosphere, the reader is referred to Le Pichon et al. (2010a). Our propagation modeling is performed initially using the 3D Hamiltonian acoustic ray-tracing code WASP-3D (Virieux et al., 2004; Dessa et al., 2005). WASP-3D models 3D acoustic propagation through atmospheric wind and temperature profiles interpolated in latitude, longitude, and altitude, utilizing a spherical geometry in order to consider earth curvature. Interpolation of the profiles in time is also possible but not used in this study because the propagation time from SP to IS44, IS45 and IS30 is shorter than the temporal resolution of the atmospheric specifications. Amplitudes are computed via paraxial rays and take into account geometrical spreading and intrinsic attenuation as a function of density and atmospheric composition (Sutherland and Bass, 2004). Ray-tracing is a high-frequency approximation to the full acoustic wavefield. Consequently, ray-tracing solutions do not account for low-frequency effects such as diffraction and scattering. Nevertheless, ray-tracing typically offers useful initial insights about infrasound propagation (e.g., Georges and Beasley, 1977).

Our atmospheric specifications consist of temperature and wind profiles from numerical weather (hindcast) predictions of the European Centre for Medium-Range Weather Forecasts (ECMWF). The ECMWF specifications consist of 91 isobar levels from 1000 to 0.01 hPa (altitude range from ~0 to ~80 km above sea level) and are provided every 3

hours. We fuse the ECMWF profiles with empirical climatologies MSIS90 (Hedin, 1991) and HWM07 (Drob et al., 2008) between altitudes of 80 to 180 km, providing seamless atmospheric profiles from 0 to 180 km altitude. Our profiles are sampled every 1° in latitude and longitude for a broad region covering the source and receiver pair, and interpolated at 200 m increments in altitude. Density and atmospheric composition are obtained from MSIS90.

In section 3.1 we first improve the source location estimates introduced in section 2.4 by applying azimuth deviation corrections predicted by ray-tracing for a point source located at SP. The source centroids obtained from this procedure are closer to the true source location than those obtained in section 2.4. However, the scatter in observed source locations is not significantly improved. In sections 3.2-3.4 we investigate atmospheric propagation from SP to IS44 in more detail. We highlight additional complexities in atmospheric propagation not captured in the ray-tracing setup of section 3.1 that may lead to scatter in source location estimates. In sections 3.2-3.4 we also investigate explanations for the systematic variations in observed wavefront parameters at IS44 shown in Figures 5 and 6 that lead to further scatter in obtained source locations.

3.1. Source re-location by cross-bearings with atmospheric correction

For each of the three stations used in the source location procedure (IS44, IS45 and IS30, Figure 7a), we calculate the azimuth deviation of rays launched from SP initially in the true direction of the stations. We use a source altitude of 1.5 km (~the peak elevation of SP) and launch rays at incidence angles between 45° and 90° from vertical with an angular separation of 1°, in both the upgoing and downgoing directions. Rays terminate when the loss (geometrical spreading and intrinsic attenuation) exceeds 180 dB. The ground surface is approximated as a flat, perfectly reflecting terrain. These calculations are repeated for every ECMWF specification available, i.e., every 3 hours, during 163-167 Julian day 2009. Rays are considered to arrive at the station when they fall within 50 km in range and 5 km in altitude of the station. Since rays travel along different trajectories to the stations, a number of phases are typically predicted at each station. By analogy with the procedures applied to the data described in section 2.4, we calculate azimuth deviation corrections from the ray simulations using: 1) the median value of azimuth deviation for all rays arriving at the station and 2) the median value of azimuth

deviation for the first rays arriving at the station. The effect of (1) is to average over all predicted phases while in (2) we isolate the predicted first-arrivals. Each method provides a single azimuth deviation correction for every 3-hour time interval for each station. At times when no rays are predicted to arrive at a station (see section 3.3), the azimuth deviation correction is zero.

Figure 7f shows the observed running median signal azimuth deviations at each station corrected with the median predicted azimuth deviation from ray-tracing (1, above). Figure 7g shows the source mis-location distance for this case. Figure 7h shows the observed first-arrival azimuth deviations corrected with the first-arrivals predicted with ray-tracing (2, above). Figure 7i shows the source mis-location distance in this second case. The source locations obtained (Figures 7l, 7m) cluster more closely around the true location of SP than the source locations obtained without atmospheric correction (Figures 7j, 7k). The mean source centroids are ~21 km and ~15 km from the true location of SP for the source location using running median and first-arrivals, respectively. However, the scatter in source locations is of the same order or worse than before (mean distance to source centroid ~38 km and ~39 km for running median and first-arrivals, respectively). This illustrates that our ray simulations can represent the mean azimuth deviations fairly accurately, however, the variability from these mean azimuth deviations is not correctly accounted for. Some of the scatter also arises when no rays are predicted at a station. In particular, at IS44, stratospheric phases are not generally predicted and thermospheric phases are only sometimes predicted (see section 3.3). Figure 7f compared to Figure 7b and Figure 7h compared to Figure 7d also illustrate that at times the atmospheric corrections under-predict or over-predict the observed azimuth deviations.

In order to improve the source location further, detailed corrections for the observed sweeps in azimuth (Figures 5 and 6) with accurate infrasonic phase prediction and identification would be necessary. In theory, the predicted azimuth deviation for each infrasonic phase could be applied to the appropriate portion of the observed signal, and the observed azimuth sweeps could be corrected. In practice, the prolonged nature of the signals makes such a detailed correction difficult to implement. However, in the following sections we highlight some features of infrasonic propagation from SP. In

addition to ray-tracing, we use an implementation of the frequency-domain Parabolic Equation (PE) method (Gibson and Norris, 2002) in order to investigate low-frequency effects, i.e., diffraction and scattering. In the following sections our modeling efforts are restricted to propagation between SP and IS44, the closest recording station. Detailed modeling of infrasonic propagation from SP to all seven observing infrasound stations is beyond the scope of the present study. The modeling results in the following sections underscore the importance of accurate atmospheric specifications, propagation modeling and source characterization (e.g., source altitude) when performing infrasonic source location.

3.2. Propagation hypotheses and HWM07

3.2.1 Diurnal variability in predicted thermospheric phases at IS44

In section 2.3 we noted that signal properties at IS44 between Julian days 163 to 164.5 are consistent with a changing variety of arriving infrasonic phases (Figures 5 and 6). One hypothesis is that the observed signal variations are caused by solar tide variability in the thermosphere (Garces et al., 2002; Le Pichon et al., 2005). Diurnal heating and wind speed changes in the thermosphere can lead to significant changes in ray turning height (Garces et al., 2002; Le Pichon et al., 2005). Since attenuation increases dramatically with altitude in the thermosphere above 100 km (Sutherland and Bass, 2004), rays that turn at lower altitude may lead us to predict signal reception at an array, whereas rays that turn at higher altitude may be highly attenuated and therefore lead us to predict signals of lower frequency or signals below noise levels at an array. Hence, the enhancement in the range of recorded trace-velocities (Figures 5, 6) may be related to a lowering of the thermospheric ray turning altitude.

Figures 8a-c show the minimum ray turning heights indicated by hourly HWM07 effective sound speed profiles for propagation from SP to IS44. The minimum ray turning heights correspond to values of effective sound speed greater than the effective sound speed at the source. HWM07 was used in Figure 8 in order to show hourly variations and since we are discussing variations in the thermosphere where ECMWF does not provide information. The effective sound speed c_{eff} (Figure 8d) is calculated by $c_{eff} = c + w_{\mathrm{prof}}$, where c is the sound speed as a function of temperature and w_{prof} is the component of wind speed in the direction of propagation. Figures 8e and f show the

temporal variations of w_{prof} and w_{cross}, where w_{cross} are the cross-profile winds with positive values approximately to southeast.

Figure 8a illustrates that the predicted minimum ray turning height in the thermosphere varies on the diurnal timescale according to HWM07. In particular, between Julian days 163.5-164, a lowering of the ray turning height is predicted, which corresponds in time with the enhanced trace-velocity deviations observed in Figures 5 and 6. We investigate this further with ray tracing in section 3.3.

3.2.2 Effect of source altitude

Figures 8a-c also illustrate another important consideration for volcanic sources. Depending on the source altitude, different infrasonic phases may propagate. In Figure 8a, for a source at 1.5 km altitude, only thermospheric phases (rays turning >100 km) are predicted. In Figure 8b, for a source at 5 km altitude, propagation in tropospheric and stratospheric ducts is also possible. For Figure 8c, for a source at 10 km altitude, stratospheric and tropospheric ducting are well defined. Rays ducting from a high-elevation source will, according to ray theory, remain in an elevated duct, with rays not necessarily reaching the ground at the receiver. However, diffraction and scattering could lead to energy propagating out of elevated stratospheric ducts and down to the ground. Considering that SP explosions produced plumes reaching to altitudes typically of 5-10 km or higher (Table 2), it is possible that the infrasonic source could be extended in altitude.

Matoza et al., (2009) proposed that broadband infrasonic tremor recorded during sustained vulcanian and plinian eruptions, such as that observed here at SP (Figure 3), may be generated by similar physical noise-generation mechanisms as those operating in man-made jet flows. It is thought that one dominant noise source in man-made jets is the growth and decay of stochastic instability waves propagating downstream along the edge of the jet flow in the shear layer between the jet flow and ambient atmosphere (Tam and Burton, 1984). A volcanic eruption column can be modeled as a lower momentum-driven jet (the gas-thrust region) that transitions with altitude into a thermally buoyant plume (Wilson, 1976; Sparks et al., 1997). Jet noise processes could operate in the lower gas-thrust portion of the eruption column. The altitude reach of the

gas-thrust region is difficult to quantify because the dynamics of the gas-thrust region are poorly understood. Factors such as air entrainment, drag force, jet expansion, multiphase interaction, and particle fallout affect the gas-thrust altitude (e.g., Self and Walker, 1994; Woods and Bower, 1995; Sparks et al., 1997; Ogden et al., 2008). Nevertheless, to a first-order, the gas-thrust altitude h may be estimated by balancing kinetic and potential energy: $h = \frac{u^2}{2g}$, where u is the vertical fluid velocity at the base of the gas-thrust region and g is the acceleration due to gravity. The velocity u may be considered an average over the cross-sectional area of the jet, downstream of the vent exit after any expansion or contraction has taken place in the fluid (i.e., after shocks if the eruption is overpressured with respect to the atmosphere (Ogden et al., 2008)). For values of u between 100 and 300 m/s (Woods and Bower, 1995), h is estimated at ~500 m to ~4.5 km altitude above the vent using energy balance. Drag force and other factors may reduce these estimates.

Above the gas-thrust region, it also remains possible that plumes could continue to generate infrasound by turbulence or other oscillations. Kanamori et al. (1994) and Kanamori (2004) proposed a model in which acoustic-gravity waves (periods >200s) are generated by thermal energy associated with volcanic eruption columns. To our knowledge, infrasound (~0.01-20 Hz) production from the plume region of a volcanic eruption column has not yet been considered. However, the gas-thrust region is probably the dominant source. This simple discussion illustrates that source elevations up to ~5 km above sea level would not be unreasonable at SP. We also note that volcanic eruptions may perturb the temperature structure of the atmosphere near the source and affect sound propagation (Fee et al., 2010a).

3.3. Ray-tracing

Figure 9 shows ray-trace simulations of propagation from SP to IS44 at three times on Julian day 163: (1) 0900 UT (Figures 9a, b), (2) 1200 UT (Figures 9c, d), and (3) 1800 UT (Figures 9e, f), (i.e., times (1), (2) and (3) on Figure 8), with two different source altitudes: 1.5 km (Figures 9a, c, and e) and 5 km (Figures 9b, d, and f). Rays were launched at incidence angles between 45° and 90° at 1° increments in the upgoing and downgoing directions, and rays terminate when the loss (geometrical spreading and

intrinsic attenuation) exceeds 180 dB. The plots in Figure 9 are 2D representations of 3D simulations (i.e., atmospheric specifications are range-dependent in Figure 9). Figures 9a, c, and e illustrate the predicted temporal variability in thermospheric arrivals at IS44 (range of 643 km). In Figure 9a (0900 UT), thermospheric returns are predicted at ranges less than and greater than 643 km, i.e., ray theory predicts that IS44 is in a thermospheric ray shadow zone. In Figure 9c, rays travel high into the thermosphere and are severely attenuated. In Figure 9e, the geometry is appropriate for thermospheric returns at IS44. The time of thermospheric predictions (1800 UT Julian day 163, Figure 9e) corresponds with the time of observed increases in trace-velocity (Figures 5 and 6). Hence, the ray simulations favor the hypothesis that the observed increases in trace-velocity (Figures 5 and 6) result from diurnal variations in the thermosphere (Figure 8). However, Figure 9a compared to Figure 9e illustrates that shadowing of thermospheric returns is important. Hence, diminution of thermospheric returns can be caused both by shadowing (Figure 9a) and by attenuation associated with increased ray turning altitude (Figure 9c). Figures 9b, d, and f illustrate the effect of an increased source altitude. In Figure 9a (source altitude 1.5 km), no stratospheric returns are predicted, while in Figure 9b (source altitude 5 km) there is propagation in an elevated stratospheric duct. Similar effects are observed in Figures 9d and f. The lack of predicted stratospheric returns at IS44 from a source at altitude 1.5 km a.s.l. (Figures 9a, c, e) is a limitation of the source re-location procedure described in section 3.1.

3.4. Parabolic equation (PE) modeling

The ray-tracing results of Figure 9 provide only a high-frequency approximation to the full propagation scenario. We investigate the importance of diffraction and scattering on infrasonic propagation from SP to IS44 using the PE software InfraMap (Gibson and Norris, 2002). Diffraction arises simply from using a more complete description of the acoustic wavefield (i.e., the PE method vs. ray-tracing). Scattering is enhanced significantly by the introduction of gravity wave (GW) perturbations (Gardner, 1994) as inhomogeneities to the effective sound speed profiles. The mean sound speed profiles used for the ray simulations of Figure 9 are shown as solid lines in Figure 10. These profiles are relatively smooth representations of the effective sound speed with altitude. In reality, gravity waves may perturb the wind field, leading to finer-scale variations in the effective sound speed (dashed lines in Figure 10). Scattering from this fine-scale

structure, coupled with diffraction, can change the propagation scenario dramatically (Kulichkov, 2010).

Figure 11 shows PE simulations of propagation from SP to IS44 on 1200 UT Julian day 163 (Time 2 in Figures 8, 9, and 10). Frequencies of 0.1 Hz and 1 Hz are used as these correspond approximately to the range of observed frequencies (Figure 6). Figure 11a shows a simulation at 1 Hz for a source at 1.5 km altitude, using the mean range-independent effective sound speed profile (solid line) in Figure 10b. When Figure 11a is compared to Figure 9c, the effects of diffraction at 1 Hz are apparent. In particular, whereas Figure 9c only shows rays terminating in the thermosphere, Figure 11a shows similar trajectories terminating in the thermosphere, but also some weak stratospheric propagation resulting from diffraction at ranges <100 km. The effect of diffraction is significantly increased at the lower frequency of 0.1 Hz (Figure 11c). In this case, diffraction results in significantly more energy predicted at IS44. Figures 11b and d differ from Figures 11a and c in having a source altitude of 5 km. Here, as also predicted by ray tracing (Figure 9d), stratospheric propagation is significantly enhanced.

Figures 11e-h show the same scenarios as Figures 11a-d respectively, except that the sound speed profiles are perturbed with one modeled realization of GW perturbations (i.e., the dashed profile in Figure 10b is used). Figures 11e-h indicate that scattering from GW perturbations has a significant effect on predictions at IS44. Scattering results in enhanced stratospheric propagation and the filling-in of ray shadow zones (Kulichkov, 2010). Increased diffraction at lower frequencies (Figures 11g-h) further enhances the effect.

4. Discussion

Large-scale explosive volcanic eruptions can inject substantial ash into the atmosphere and disrupt air traffic. The June 2009 SP eruption and its ash clouds resulted in 65 flight re-routes, 6 diversions, 2 turn-backs to original departure cities, and 12 unscheduled fuel stops (Salinas, 2010). Since seismic network coverage is sparse in the Kurils, infrasound arrays represent a promising means to enhance volcanic monitoring in the region. Red triangles in Figure 7a represent the position of Holocene volcanoes (Siebert and Simkin, 2002-). The obtained scatter in infrasound source location estimates of up

to ~100 km (Figure 7) indicates the possible accuracy of automated source location procedures using the current IMS station configuration in the Kurils. The scatter of ~100 km may lead to some minor ambiguity as to which particular volcano may have erupted (compare source locations with red triangles in Figures 7a, j-m). However, a source location with error of ~100 km could still provide useful information to trigger a search of satellite data or to inform ash dispersal forecast models. In addition, the timing and duration of eruption (Figure 4) are parameters that may be readily estimated from infrasonic data. Therefore, existing IMS station coverage is already adequate to provide useful information about large-scale explosive volcanism in certain regions such as the Kurils. However, the intensity of volcanic explosions detectable by the IMS infrasound network will vary spatially and temporally, as a function of station density, ambient noise conditions and variability in the atmosphere (Le Pichon et al., 2009). Thus, any infrasound volcanic monitoring program should give careful consideration to the infrasound network detection capability. The IMS infrasound station density is higher in the Kurils region compared to other volcanic regions (e.g., IMS station density is lower in the Caribbean and Central America; Christie and Campus, 2010). It is anticipated that if the infrasound station density in a region increases, the infrasound network detection capability will increase and the source location error and ambiguity in volcano location will also be reduced.

The explosion chronology determined from infrasound data (Table 1), provides an independent constraint on the eruption chronology compiled using satellite data (Table 2). Comparison of the two chronologies is relatively straightforward when explosions occur isolated in time (e.g., after Julian day 164.5 on Figure 4). However, comparison between the two chronologies requires a higher level of interpretation when the infrasound detections occur continuously or with short inter-event times (e.g., between Julian day 163 and 164.5 on Figure 4). The explosion onset times in Table 2 were estimated from the time when a dense ash cloud is first visible in satellite data (TERRA, NOAA, MTSAT) above the meteorological cloud layer. In addition to the activity identified in Table 2, continuous ash and gas-steam emissions were also observed in satellite data during the eruption, e.g., between Julian day 163 and 164.5. Closely spaced explosions could feed a single sustained eruption column (e.g., Sparks et al., 1997). In addition, pyroclastic flows can generate infrasound (e.g., Yamasato, 1997; Ripepe et al.,

2009) and not all explosions that generate infrasound produce ash (e.g., Garces et al., 2008; Fee et al., 2010b). Therefore, we do not necessarily expect a one-to-one correlation between infrasound signal detections (Table 1), and visual satellite observation of plumes (Table 2, Figure 4). Furthermore, low-amplitude source activity may not register on remote infrasound stations and weak explosions reaching less than ~3 km in altitude may not have been visible in satellite data due to near-continuous cloud cover during the eruption. Nevertheless, the infrasound signal detections provide a continuous, high temporal resolution chronology of the volcanic source that may be compared with satellite data (Figure 4).

Our array observations of the June 2009 SP eruption are consistent with infrasonic arrivals consisting of a mix of idealized tropospheric, stratospheric and thermospheric phases (Figures 2, 5, 6). The overlapping nature of the arrivals can be explained by a long-duration source-time function at SP (e.g., a sustained, long-duration jetting signal), convolved with atmospheric propagation response. The effects of temporal changes in atmospheric propagation are evident in trace-velocity and azimuth deviation variations observed between Julian days 163-164.5 2009. Using preliminary modeling of infrasound propagation between SP and IS44, we attribute these trace-velocity variations to diurnal variability in the thermosphere. We note that Fee et al., (2010a) modeled infrasound propagation from Kasatochi volcano, Aleutians, and similarly found that, for some explosions, ray-tracing and parabolic equation modeling predicted only thermospheric phases, whereas the observed infrasonic arrival times were more consistent with stratospheric ducting. Our simulations illustrate three possible ways to enhance stratospheric ducting: 1) extended acoustic source altitude, 2) diffraction, and 3) scattering of infrasound by atmospheric inhomogeneities.

5. Conclusions

The June 2009 eruption of SP produced significant infrasound that was recorded on six stations of the IMS infrasound network and several stations of the KIGAM infrasound network at ranges of ~640-6,400 km. Signals at the three closest recording stations IS44 (643 km), IS45 (1,690 km), and IS30 (1,774 km) represent a detailed record of the explosion chronology that correlates well with an eruption chronology compiled by SVERT based on satellite data. However, the infrasound data appear to provide a more

detailed (i.e., higher temporal resolution) eruption chronology than is possible with satellite data alone. Infrasonic source locations determined from running median backazimuth cross-bearings from the three closest stations have a mean source centroid ~33 km from the true location of SP when no atmospheric propagation correction is applied. This distance reduces to ~15 km using infrasonic first-arrivals and an atmospheric propagation correction based on 3D ray-tracing and numerical weather hindcast predictions. However, scatter in source locations of up to ~100 km result from details of atmospheric propagation that are currently unresolved. For instance, observed arrivals consistent with stratospheric phases are not predicted with the ray simulations at IS44 for a source at 1.5 km altitude a.s.l.. In addition, systematic variations in trace-velocity, backazimuth deviation, and signal frequency content are observed at IS44, which may be explained by a long-duration source-time function convolved with atmospheric propagation response. Preliminary investigation of atmospheric propagation from SP to IS44 indicates that these observed variations in wavefront parameters can be attributed to solar tide variability in the thermosphere. We also showed that the geometry and duration of the source, diffraction, and scattering from atmospheric inhomogeneities are important when considering infrasound observations from explosive volcanic sources. We have demonstrated the utility of the existing IMS infrasound network for remote monitoring of the Kurils. Significant improvements in the ability to monitor the Kurils with infrasound could be gained by additional array deployments in the region. Ongoing research on the propagation and location of atmospheric infrasound may also lead to substantial improvements in infrasound monitoring of remote volcanic regions.

Acknowledgments

We thank Lars Ceranna, David Fee and David Green for their helpful comments and suggestions, and Darcy Ogden for discussion about gas-thrust altitude. ECMWF data were provided by the PTS of the CTBTO. This manuscript was improved after comments from an anonymous reviewer and Jeffrey Johnson.

References

Bass, H.E., 1991. Atmospheric acoustics, in *Encyclopedia of Applied Physics*, Volume 2, 145-179, VCH, New York.

Brown, D.J., Katz, C.N., Le Bras, R., Flanagan, M.P., Wang, J. and Gault, A.K., 2002. Infrasonic signal detection and source location at the Prototype International Data Centre. *Pure Appl. Geophys.*, 159(5): 1081-1125.

Cansi, Y., 1995. An automatic seismic event processing for detection and location – the PMCC method. *Geophys. Res. Lett.*, 22(9): 1021-1024.

Ceranna, L., Le Pichon, A., Green, D.N. and Mialle, P., 2009. The Buncefield explosion: a benchmark for infrasound analysis across Central Europe. *Geophys. J. Int.*, 177(2): 491-508.

Christie, D.R. and Campus, P., 2010. The IMS Infrasound Network: Design and Establishment of Infrasound Stations In: A. Le Pichon, E. Blanc and A. Hauchecorne (Editors), Infrasound Monitoring for Atmospheric Studies. Springer Netherlands, pp. 29-75.

DeFatta, D., Lucas, J., and Hodgkiss, W., 1988. Digital signal processing: A system design approach, John Wiley, New York.

Dessa, J.X., Virieux, J. and Lambotte, S., 2005. Infrasound modeling in a spherical heterogeneous atmosphere. *Geophys. Res. Lett.*, 32(12): 5.

Drob, D.P., Picone, J.M. and Garces, M., 2003. Global morphology of infrasound propagation. *J. Geophys. Res.-Atmos.*, 108(D21): 12.

Drob, D.P., Emmert, J.T., Crowley, G., Picone, J.M., Shepherd, G.G., Skinner, W., Hays, P., Niciejewski, R.J., Larsen, M., She, C.Y., Meriwether, J.W., Hernandez, G., Jarvis, M.J., Sipler, D.P., Tepley, C.A., O'Brien, M.S., Bowman, J.R., Wu, Q., Murayama, Y., Kawamura, S., Reid, I.M. and Vincent, R.A., 2008. An empirical model of the Earth's horizontal wind fields: HWM07. *J. Geophys. Res-Space Phys.*, 113(A12): 18.

Evers, L.G. and Haak, H.W., 2005. The detectability of infrasound in the Netherlands from the Italian volcano Mt. Etna. *J. Atmos. Sol.-Terr. Phys.*, 67(3): 259-268.

Evers, L.G. and Haak, H.W., 2007. Infrasonic forerunners: Exceptionally fast acoustic phases, *Geophys. Res. Lett.,* 34, L10806, doi:10.1029/2007GL029353

Fee, D., Steffke, A., Garces, M., 2010a Characterization of the 2008 Kasatochi and Okmok eruptions using remote infrasound arrays, *J. Geophys. Res.*, 115, D00L10, doi: 10.1029/2009JD013621.

Fee, D., Garces, M., Steffke, A., 2010b. Infrasound from Tungurahua Volcano 2006-2008: Strombolian to Plinian Eruptive Activity, *J. Volcanol. Geotherm. Res.*, 193 (1-2), 67-81.

Garces, M.A., Hansen, R.A. and Lindquist, K.G., 1998. Traveltimes for infrasonic waves propagating in a stratified atmosphere. *Geophys. J. Int.*, 135(1): 255-263.

Garces, M., Drob, D.P. and Picone, J.M., 2002. A theoretical study of the effect of geomagnetic fluctuations and solar tides on the propagation of infrasonic waves in the upper atmosphere. *Geophys. J. Int.*, 148(1): 77-87.

Garces, M., Fee, D., Steffke, A. McCormack, D., Servranckx, R., Bass, H., Hetzer, C., Hedlin, M., Matoza, R., Yepes, H., Ramon, P., 2008. Capturing the Acoustic Fingerprint of Stratospheric Ash Injection, *Eos Trans. AGU*, 89(40), doi:10.1029/2008EO400001.

Gardner, C.S., 1994. Diffusive filtering theory of gravity wave spectra in the atmosphere. *J. Geophys. Res.-Atmos.*, 99(D10): 20,601-20622.

Georges, T.M. and Beasley, W.H., 1977. Refraction of infrasound by upper-atmospheric winds. *J. Acoust. Soc. Am.*, 61(1): 28-34.

Gibson, R. G., and Norris, D. E., 2002. Development of an infrasound propagation modeling tool kit, DTRA-TR-99–47, Defense Threat Reduction Agency, Fort Belvoir, VA, 22060-6201.

Hedin, A.E., 1991. Extension of the MSIS thermosphere model into the middle and lower atmosphere. *J. Geophys. Res-Space Phys.*, 96(A2): 1159-1172.

Kanamori, H., 2004. Some fluid-mechanical problems in geophysics - waves in the atmosphere and fault lubrication. *Fluid Dyn. Res.*, 34(1): 1-19.

Kanamori, H., Mori, J. and Harkrider, D.G., 1994. Excitation of atmospheric oscillations by volcanic eruptions. *J. Geophys. Res.*, 99(B11): 21947-21961.

Kulichkov, S. N., Avilov, K. V., Bush, G. A., Popov, O. E., Raspopov, O. M., Baryshnikov, A. K., ReVelle, D. O. and Whitaker, R. W., 2004. On anomalously fast infrasonic arrivals at long distances from surface explosions, *Izv. Russ. Acad. Sci. Atmos. Oceanic Phys.*, *Engl. Transl.*, 40, 1–9.

Kulichkov, S., 2010. On the prospects for acoustic sounding of the fine structure of the middle atmosphere, in Le Pichon, A., Blanc, E., Hauchecorne, A., (Eds.), *Infrasound monitoring for atmospheric studies*, 1st edition, Springer, ISBN: 978-1-4020-9507-8.

Le Pichon, A., Blanc, E., Drob, D., Lambotte, S., Dessa, J.X., Lardy, M., Bani, P. and Vergniolle, S., 2005. Infrasound monitoring of volcanoes to probe high-altitude winds. *J. Geophys. Res.-Atmos.*, 110(D13): 12.

Le Pichon, A., Vergoz, J., Herry, P. and Ceranna, L., 2008. Analyzing the detection capability of infrasound arrays in Central Europe. *J. Geophys. Res.-Atmos.*, 113(D12): 9.

Le Pichon, A., Vergoz, J., Blanc, E., Guilbert, J., Ceranna, L., Evers, L. and Brachet, N., 2009. Assessing the performance of the International Monitoring System's infrasound network: Geographical coverage and temporal variabilities. *J. Geophys. Res.-Atmos.*, 114: 15.

Le Pichon, A., Blanc, E., Hauchecorne, A., (Eds.), 2010a. Infrasound monitoring for atmospheric studies, 1st edition, Springer, ISBN: 978-1-4020-9507-8.

Le Pichon, A., Matoza, R., Brachet, N. and Cansi, Y., 2010b, Recent enhancements of the PMCC infrasound signal detector, *Inframatics*, September 2010 issue.

Matoza, R.S., 2009. Seismic and infrasonic source processes in volcanic fluid systems. Ph.D. Dissertation, University of California, San Diego.

Matoza, R.S., Fee, D., Garces, M.A., Seiner, J.M., Ramon, P.A. and Hedlin, M.A.H., 2009. Infrasonic jet noise from volcanic eruptions. Geophys. Res. Lett., 36:5.

Neal, C., Girina, O., Senyukov, S., Rybin, A., Osiensky, J., Izbekov, P. and Ferguson, G., 2009. Russian eruption warning systems for aviation. *Nat. Hazards*, 51(2): 245-262.

Ogden, D.E., Glatzmaier, G.A. and Wohletz, K.H., 2008. Effects of vent overpressure on buoyant eruption columns: Implications for plume stability. *Earth Planet. Sci. Lett.*, 268(3-4): 283-292.

Ripepe, M., De Angelis, S., Lacanna, G., Poggi, P., Williams, C., Marchetti, E., Delle Donne, D. and Ulivieri, G., 2009. Tracking pyroclastic flows at Soufrière Hills Volcano, *Eos Trans. AGU*, 90(27), doi:10.1029/2009EO270001.

Salinas, L.J., 2010. United Airlines Flight Dispatch, Congressional Hazards Caucus Alliance (http://www.agiweb.org)

Self, S. and Walker, G.P.L., 1994, Ash clouds: characteristics of eruption columns In: T.J. Casadevall (Editor), Volcanic Ash and Aviation Safety: Proceedings of the First International Symposium on Volcanic Ash and Aviation Safety, U.S. Geological Survey Bulletin 2047, pp. 65-74.

Siebert L. and Simkin T (2002-). Volcanoes of the World: an Illustrated Catalog of Holocene Volcanoes and their Eruptions. Smithsonian Institution, Global Volcanism Program Digital Information Series, GVP-3, (http://www.volcano.si.edu/world/).

Sparks, R.S.J., Burski, M.I., Carey, S.N., Gilbert, J.S., Glaze, L.S., Sigurdsson, H. and Woods, A.W., 1997. Volcanic Plumes. Wiley-Blackwell.

Sutherland, L.C. and Bass, H.E., 2004. Atmospheric absorption in the atmosphere up to 160 km. *J. Acoust. Soc. Am.*, 115(3): 1012-1032.

SVERT (Sakhalin Volcanic Eruptions Response Team) (2009), Widespread plumes from large 11-16 June 2009 eruption, *Bulletin of the Global Volcanism Network*, Monthly report 06/2009, 34:06, Smithsonian Global Volcanism Program, (http://www.volcano.si.edu/world)

Szuberla, C.A.L. and Olson, J.V., 2004. Uncertainties associated with parameter estimation in atmospheric infrasound arrays. *J. Acoust. Soc. Am.*, **115**, 1, 253-258.

Tam, C.K.W. and Burton, D.E., 1984. Sound generated by instability waves of supersonic flows 2. Axisymmetric jets. *J. Fluid Mech.*, 138(JAN): 273-295.

Virieux, J., Garnier, N., Blanc, E. and Dessa, J.X., 2004. Paraxial ray tracing for atmospheric wave propagation. *Geophys. Res. Lett.*, 31(20): 5.

Willis, M., Garces, M., Hetzer, C. and Businger, S., 2004. Infrasonic observations of open ocean swells in the Pacific: Deciphering the song of the sea. *Geophys. Res. Lett.*, 31(19): 4.

Wilson, L., 1976. Explosive volcanic eruptions 3. Plinian eruption columns. *Geophysical Journal of the Royal Astronomical Society*, 45(3): 543-556.

Woods, A.W. and Bower, S.M. 1995. The decompression of volcanic jets in a crater during explosive volcanic eruptions. *Earth Planet Sci. Lett.* 131(3-4): 189-205.

Yamasato, H., 1997. Quantitative analysis of pyroclastic flows using infrasonic and seismic data at Unzen volcano, Japan. *J. Phys. Earth*, 45(6): 397-416.

Figure Captions

Figure 1

Map showing location of Sarychev Peak (SP, red triangle), infrasound arrays that recorded signal from SP (blue inverted triangles), and infrasound arrays that did not record signal from SP (black inverted triangles). Signals are observed at long-range to the west of SP corresponding to the stratospheric downwind direction in June 2009. Inset: Astronaut photograph of SP eruption column taken at 22:16 UT 12 June 2009 from the International Space Station (ISS). Image credit: NASA's Earth Observatory.

Figure 2

PMCC processing of 10 infrasound arrays deployed globally (see Figure 1). Arrays are shown in order of increasing range from SP. Detections are displayed in terms of their backazimuth deviation from the true great-circle path from each array to SP (azimuth scale is constant for all stations). Color bar corresponds to log_{10} (N) where N is the number of PMCC pixels in a bin of size 0.1° in azimuth and 3.5 minutes in time. Detections at each station have been aligned in time back to an assumed origin time at SP by time-shifting the infrasonic arrivals by a celerity of 0.33 km/s. Clear infrasonic detections from the entire SP sequence are recorded at IS44 (range from SP r = 643 km), IS45 (1,690 km), IS30 (1,774 km), and YAG (2,310 km). Infrasonic detections from various individual explosions within the entire sequence are also recorded further away at IS34 (3,450 km), IS46 (4,655 km) and IS31 (6,433 km) (indicated by arrows). No detections are recorded at IS53, IS39 and IS59.

Figure 3

Infrasonic waveforms recorded at IS44 (Kamchatka) for the entire SP eruption sequence (5 days: 11-16 June 2009, or Julian days 162-167 2009). Each waveform shows one full day of data. E.g., Origin time of upper trace: 0000 UT 11 June 2009 (day 162). Origin time of lower trace: 0000 UT 15 June 2009 (day 166). Infrasound array data have been beamformed (waveforms aligned and stacked for azimuth of SP and acoustic velocity) using a time-delay beamformer and filtered 0.5-5 Hz. Note that some of the features observed on this plot are local wind noise and not coherent infrasonic signal (refer to Figure 2).

Figure 4

Chronology of coherent infrasonic signal at IS44 compared to the eruption chronology inferred from satellite data by SVERT. Lower plot: number of PMCC detections per minute at IS44 originating from the direction of SP. Time of arrivals are corrected back to an inferred origin time at Sarychev assuming a celerity of 0.33 km/s. Black horizontal bars above plot represent beginning and end times of coherent signal packets. Grey bars represent explosion onset times +/-15 minutes inferred from satellite data by SVERT. Vertical extent of each grey bar is scaled relative to the maximum plume altitude inferred by SVERT. Upper plot: an expanded view of lower plot between Julian days 163-164.5 2009.

Figure 5

Detail of observed (a) azimuth and (b) trace-velocity deviations at IS44, IS45, and IS30 between Julian days 163-164.5 2009. Azimuth deviations in (a) are from the true great circle path azimuth to SP. Trace-velocity deviations in (b) are from a sound speed of 0.34 km/s. Color bar corresponds to $log_{10}(N)$ where N is the number of PMCC pixels in a bin of size 1.5 minutes in time and (a) 0.05° in azimuth and (b) 0.3 m/s in trace-velocity.

Figure 6

Detail of observed (a) trace-velocity, (b) dominant frequency, and (c) azimuth deviations at IS44. (d, e, f) as (a, b, c) but for IS45. The dominant frequency (b, e) was estimated by an automatic procedure that beamforms the raw signal data at the azimuth and trace-velocity of each PMCC family.

Figure 7

Infrasonic source location via backazimuth cross-bearings using three stations: IS44, IS45, and IS30. Four different source location procedures are compared. In b, c, and j, source location is performed on a running median of the observed signal azimuth and no atmospheric propagation correction is applied. In d, e, and k, source location is performed on infrasonic first-arrivals and no atmospheric propagation correction is applied. In f, g, and l, source location is performed on a running median of the observed signal and a backazimuth correction is applied. In h, i, and m, source location is performed on infrasonic first-arrivals and a backazimuth correction is applied. The

backazimuth correction used in f, g, l and h, i, m is calculated by ray-tracing with ECMWF, HWM07, and MSIS90 (see section 3.1). (a) Location of the three stations (inverted blue triangles) relative to SP (large red triangle). Other small red triangles are Holocene volcanoes (Siebert and Simkin, 2002-). Dashed lines are the true great circle path azimuths from each station to SP. Box indicates area of j-m. (b, d, f, h) Signal azimuth deviation at the three stations (black: IS44, red: IS45, blue: IS30). Times are corrected for a constant celerity of 0.33 km/s. (c, e, g, i) Source location error: distance (km) between true SP location and the obtained infrasonic source locations. The dot colors are varied with time to facilitate comparison with j-m. (j-m) Source locations (dots) and the true position of SP (large red triangle). The source location dots are colored as a function of time (see c, e, g, i). The mean source centroid in each case is shown as a black star. Dashed ellipse shows 90 % confidence for source location assuming azimuth errors normally distributed around true with a standard deviation of 3°.

Figure 8

Temporal variability of HWM07 effective sound speed c_{eff}, wind and predicted minimum ray turning heights for propagation from SP to IS44. (a) Minimum ray turning height for a source at 1.5 km altitude. Cross-hatched regions correspond to values of c_{eff}/c_{eff}(source) >1, while blank regions correspond to values of c_{eff}/c_{eff}(source) <1. Rays may turn back towards the ground in the cross-hatched regions. (b) As (a) but for a source at 5 km altitude. (c) as (a) but for a source at 10 km altitude. (d) Effective sound speed variations from which (a-c) were obtained. (e), (f) in-profile and cross winds respectively. Dashed vertical lines represent times when ECMWF profiles are also available. Times (1), (2), and (3) indicated at top of figure correspond to: (1) 0900 UT, (2) 1200 UT, and (3) 1800 UT on Julian day 163. These times correspond to simulations and profiles shown in Figures 9, 10 and 11.

Figure 9

WASP-3D ray-trace simulations of propagation from SP to IS44 on Julian day 163. (a) 0900 UT, source altitude 1.5 km, (b) 0900 UT, source altitude 5 km, (c) 1200 UT, source altitude 1.5 km, (d) 1200 UT, source altitude 5 km, (e) 1800 UT, source altitude 1.5 km, (f) 1800 UT, source altitude 5 km. Rays terminate when the loss exceeds 180 dB. Note

the variations in thermospheric returns at IS44 (range 643 km) with time (compare a, c, e), and the enhanced possibility of stratospheric propagation for increased source altitude (compare b to a; d to c; f to e).

Figure 10

Mean effective sound speed profiles (solid lines) along a great-circle path from SP to IS44 at (a) 0900 UT, (b) 1200 UT, and (c) 1800 UT Julian day 163. These times correspond respectively to times (1), (2), and (3) on Figure 8. Dashed lines show the effective sound speed profiles when perturbed by a single modeled realization of gravity waves (Gardner, 1994).

Figure 11

Parabolic equation (PE) simulations of propagation from SP to IS44 at 1200 UT Julian day 163. Loss in dB (including intrinsic attenuation) is referenced to a distance of 1 km from the source. The simulations investigate the effects of frequency (f = 0.1 Hz, 1 Hz), source altitude (z_s = 1.5 km, 5 km) and gravity wave (GW) perturbations (Gardner, 1994). (a) f = 1 Hz, z_s = 1.5 km, no GWs. (b) f = 1 Hz, z_s = 5 km, no GWs. (c) f = 0.1 Hz, z_s = 1.5 km, no GWs. (d) f = 0.1 Hz, z_s = 5 km, no GWs. (e) f = 1 Hz, z_s = 1.5 km, with GWs. (f) f = 1 Hz, z_s = 5 km, with GWs. (g) f = 0.1 Hz, z_s = 1.5 km, with GWs. (h) f = 0.1 Hz, z_s = 5 km, with GWs.

Table 1: Infrasonic signal chronology determined for IS44.

Inferred origin time at SP	t_on at IS44	t_off at IS44	Duration (min)	Dominant Period (s)	Amplitude (Pa)
2009-06-11 05:38	2009-06-11 06:11	2009-06-11 06:16	5	1.60	0.013
2009-06-11 06:38	2009-06-11 07:11	2009-06-11 07:17	6	0.50	0.029
2009-06-11 07:43	2009-06-11 08:16	2009-06-11 08:22	6	0.80	0.010
2009-06-12 01:38	2009-06-12 02:11	2009-06-12 04:08	117	3.60	0.045
2009-06-12 03:51	2009-06-12 04:24	2009-06-12 04:36	13	1.00	0.026
2009-06-12 04:18	2009-06-12 04:51	2009-06-12 05:04	13	1.50	0.023
2009-06-12 04:44	2009-06-12 05:17	2009-06-12 05:28	12	1.65	0.040
2009-06-12 05:07	2009-06-12 05:40	2009-06-12 05:54	14	1.80	0.041
2009-06-12 05:29	2009-06-12 06:02	2009-06-12 06:21	19	2.00	0.053
2009-06-12 05:50	2009-06-12 06:23	2009-06-12 06:45	22	2.90	0.044
2009-06-12 06:18	2009-06-12 06:51	2009-06-12 07:16	24	2.00	0.045
2009-06-12 06:48	2009-06-12 07:21	2009-06-12 08:37	76	2.70	0.036
2009-06-12 08:13	2009-06-12 08:46	2009-06-12 09:26	40	2.50	0.037
2009-06-12 08:59	2009-06-12 09:32	2009-06-12 10:00	28	2.00	0.020
2009-06-12 09:30	2009-06-12 10:03	2009-06-12 10:15	12	2.10	0.026
2009-06-12 09:46	2009-06-12 10:19	2009-06-12 11:20	62	1.15	0.016
2009-06-12 10:52	2009-06-12 11:25	2009-06-12 11:38	13	2.20	0.028
2009-06-12 11:25	2009-06-12 11:58	2009-06-12 12:04	6	1.00	0.011
2009-06-12 11:33	2009-06-12 12:06	2009-06-12 12:12	6	1.80	0.020
2009-06-12 11:57	2009-06-12 12:30	2009-06-12 12:40	11	0.85	0.012
2009-06-12 12:28	2009-06-12 13:01	2009-06-12 13:05	4	1.05	0.031
2009-06-12 12:55	2009-06-12 13:28	2009-06-12 13:38	10	0.90	0.013
2009-06-12 13:36	2009-06-12 14:09	2009-06-12 14:15	6	0.90	0.029
2009-06-12 14:07	2009-06-12 14:40	2009-06-12 14:51	12	1.20	0.028
2009-06-12 14:51	2009-06-12 15:24	2009-06-12 15:39	16	2.10	0.031
2009-06-12 15:38	2009-06-12 16:11	2009-06-12 16:25	15	2.80	0.031
2009-06-12 16:13	2009-06-12 16:46	2009-06-12 17:10	24	5.15	0.043
2009-06-12 17:00	2009-06-12 17:33	2009-06-12 17:58	25	5.50	0.069
2009-06-12 17:46	2009-06-12 18:19	2009-06-12 18:44	25	5.20	0.080
2009-06-12 18:38	2009-06-12 19:11	2009-06-12 19:34	23	5.40	0.061
2009-06-12 19:32	2009-06-12 20:05	2009-06-12 20:22	17	4.40	0.084
2009-06-12 20:29	2009-06-12 21:02	2009-06-12 21:24	22	4.50	0.076
2009-06-12 22:14	2009-06-12 22:47	2009-06-12 23:06	20	4.45	0.093
2009-06-12 23:16	2009-06-12 23:49	2009-06-13 00:11	22	2.85	0.064
2009-06-13 00:57	2009-06-13 01:30	2009-06-13 01:51	22	1.40	0.058
2009-06-13 01:57	2009-06-13 02:30	2009-06-13 03:17	48	2.85	0.081
2009-06-13 04:53	2009-06-13 05:26	2009-06-13 06:20	55	3.50	0.108
2009-06-13 09:27	2009-06-13 10:00	2009-06-13 10:34	34	1.80	0.029
2009-06-13 21:30	2009-06-13 22:03	2009-06-13 22:53	50	5.20	0.174
2009-06-14 18:51	2009-06-14 19:24	2009-06-14 20:43	79	7.00	0.235
2009-06-15 01:15	2009-06-15 01:48	2009-06-15 02:27	39	7.95	0.241
2009-06-15 09:18	2009-06-15 09:51	2009-06-15 10:26	35	4.40	0.209
2009-06-15 11:37	2009-06-15 12:10	2009-06-15 12:37	27	6.80	0.103
2009-06-15 16:43	2009-06-15 17:16	2009-06-15 17:56	40	6.60	0.270

Table 2: Eruption chronology of Sarychev Peak 11-16 June 2009 inferred from satellite data and analysis at SVERT.

Explosion №	Date	Time (UTC)	Height	Direction and length of ash plumes (visible)
1	11.06	02:00	3 km	Weak ash emission.
2	11.06	07:00	4 km	Weak ash emission.
3	12.06	02:00	10 km	125 km to the east.
4	12.06	04:00	6 km	370 km to the southeast and 25 km to the west.
5	12.06	07:57	12 km	200 km to the southeast and 185 km to the west.
6	12.06	14:57	5 km	225 km to the southeast and 210 km to the west.
7	12.06	17:13	5 km	240 km to the southeast and 225 km to the west. Width of the plume is 85 km.
8	12.06	18:57	5 km	350 km to the southeast and 225 km to the southwest. Width of the plume is 150 km.
9	12.06	22:15	5 km	>500 km to the southeast, > 200 km to the southwest. Width of the plume is 205 km.
10	12.06	23:30	6 km	>500 km to the southeast, > 200 km to the southwest. Width of the plume is 205 km.
11	13.06	01:30	10 km	>500 km to the southeast, > 200 km to the southwest. Width of the plume is 205 km.
12	13.06	04:30	10 km	Main direction of the plume is to the southeast, >500 km
13	13.06	04:50	10 km	Main direction of the plume is to the southeast, >500 km
14	13.06	09:30	10 km	Main direction of the plume is to the southeast, >500 km, width ~200 km
15	13.06	21:30	21 km	>500 km to the southeast with width 210 km; >300 km to the northwest
16	14.06	18:50	16 km	>500 km to southeast with width 250 km; >300 km to the northwest
17	15.06	00:57	12 km	>400 km to the east, ~300 km to the west
18	15.06	05:15	5 km	>550 km to the southeast and >600 km to the northwest
19	15.06	09:20	10 km	>600 km to the southeast and >800 km to the northwest
20	15.06	10:25	10 km	>600 km to the southeast and >800 km to the northwest
21	15.06	10:55	16 km	>600 km to the southeast and >800 km to the northwest
22	15.06	16:55	10 km	>600 km to the southeast and >800 km to the northwest
23	16.06	20:45	5 km	>600 km to the southeast and >800 km to the northwest

Figure 1
Click here to download Figure: figure_1.eps

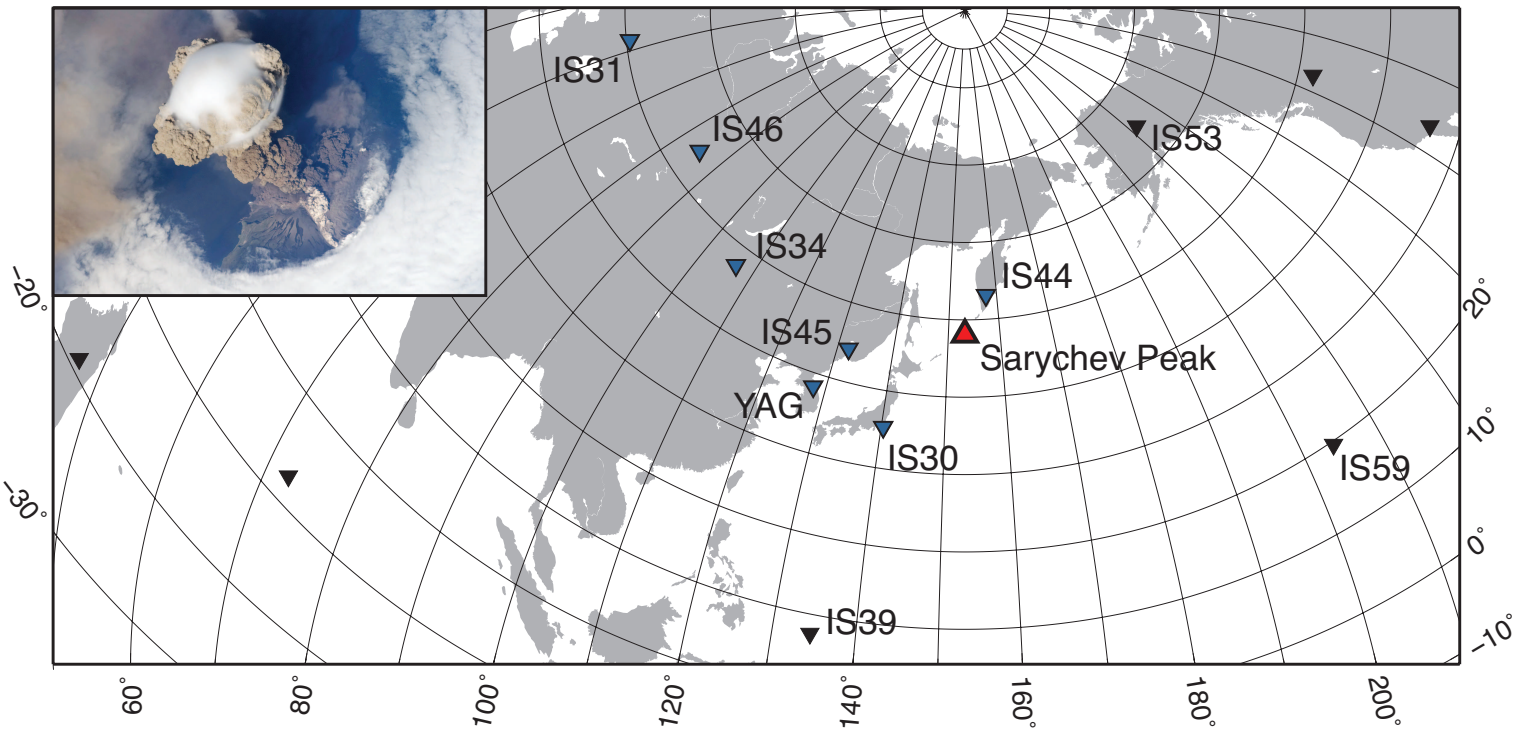

Figure 2
Click here to download Figure: figure_2.eps

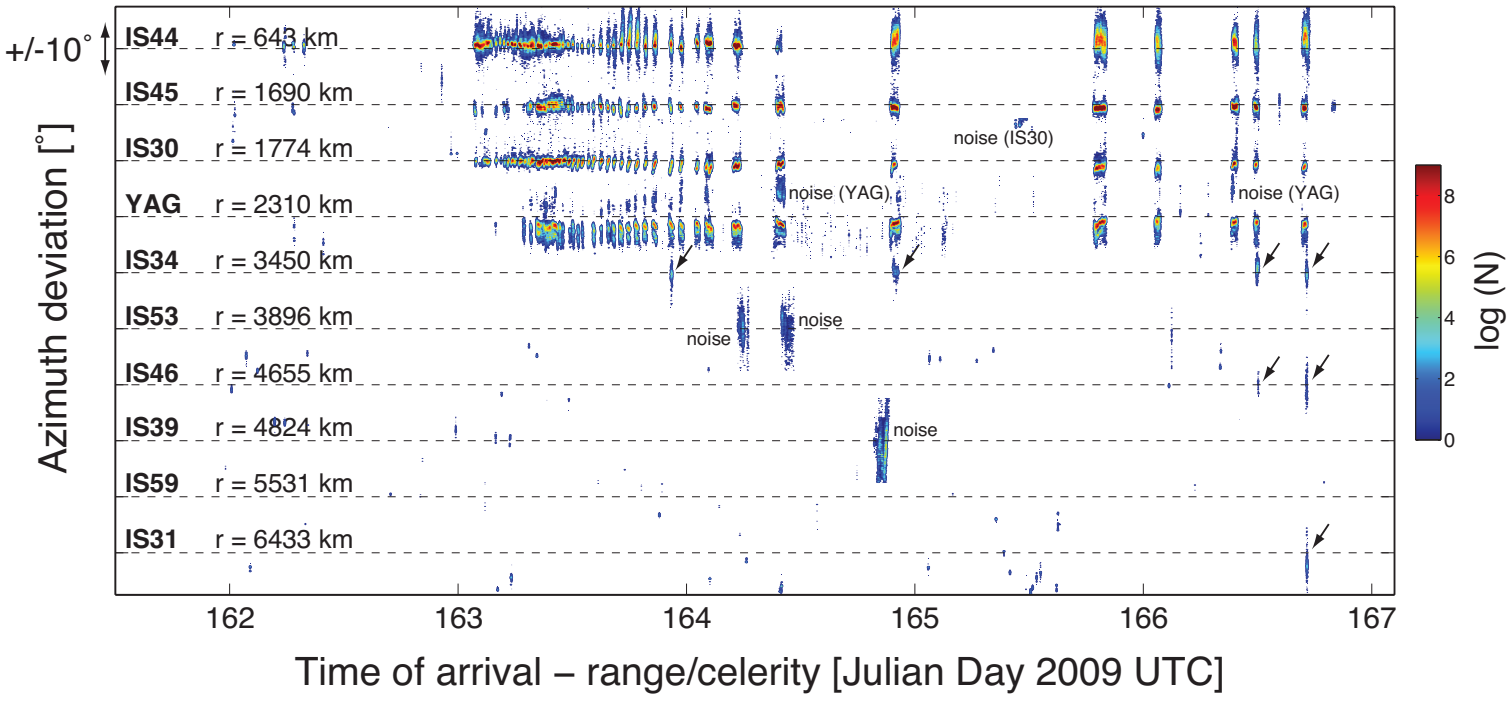

Figure 3

Click here to download Figure: figure_3.pdf

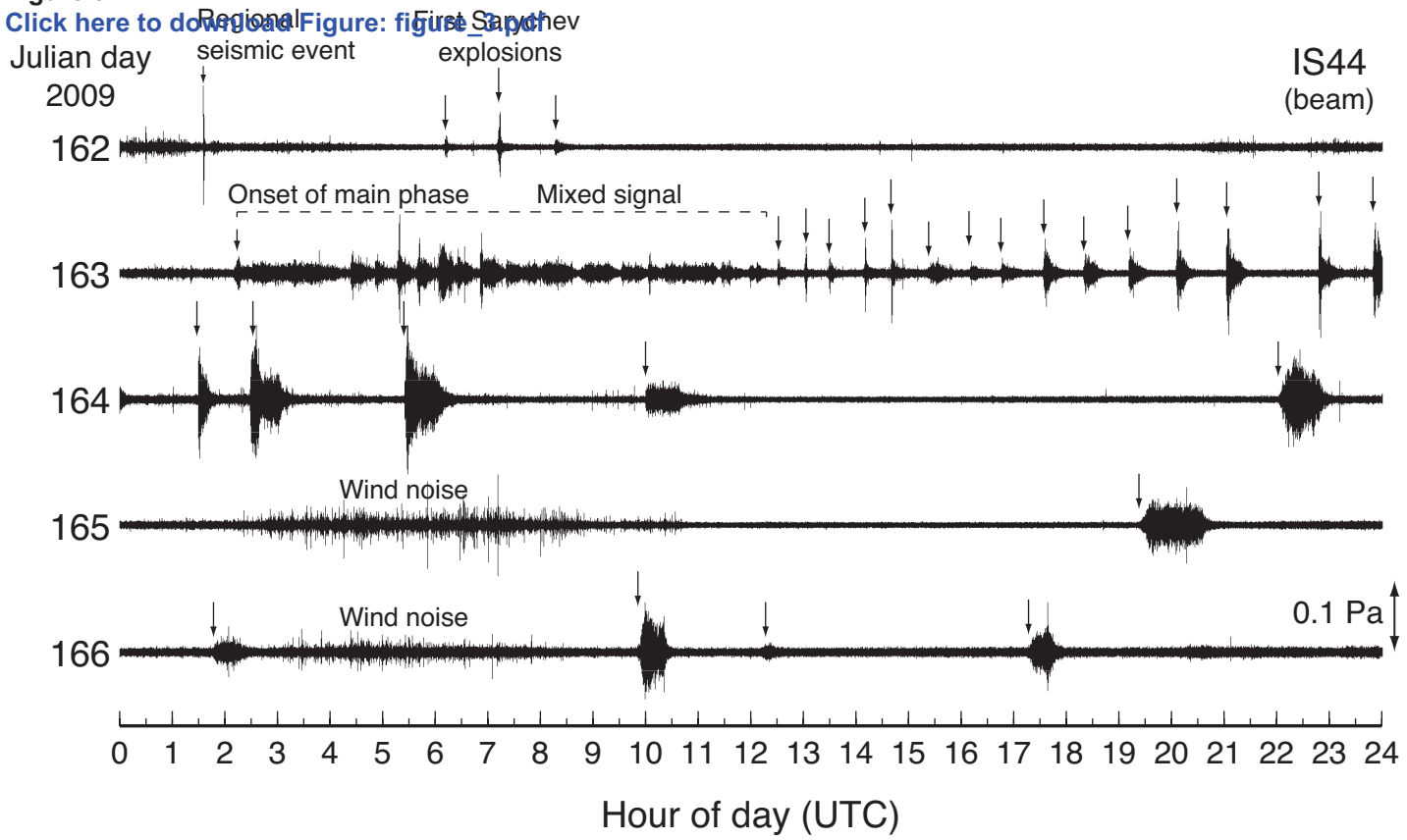

Figure 4
Click here to download Figure: figure_4.eps

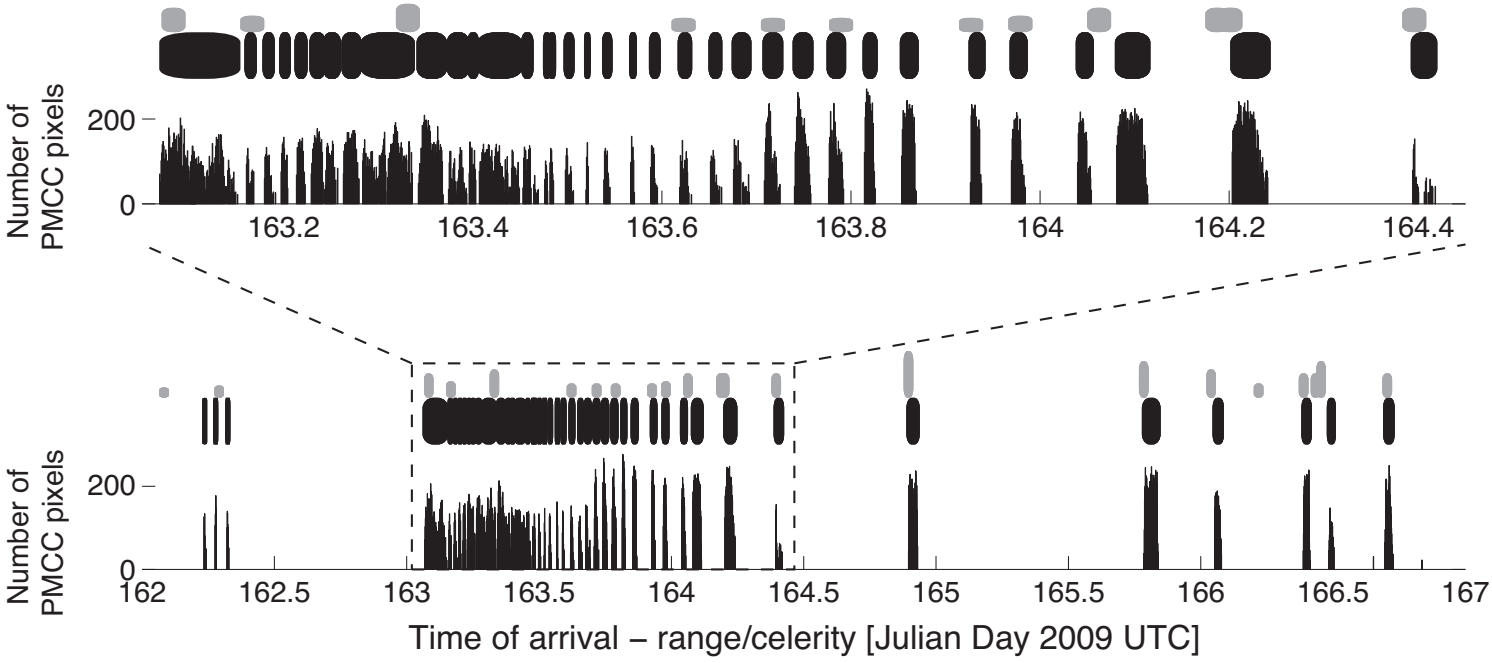

Figure 5
Click here to download Figure: figure_5.eps

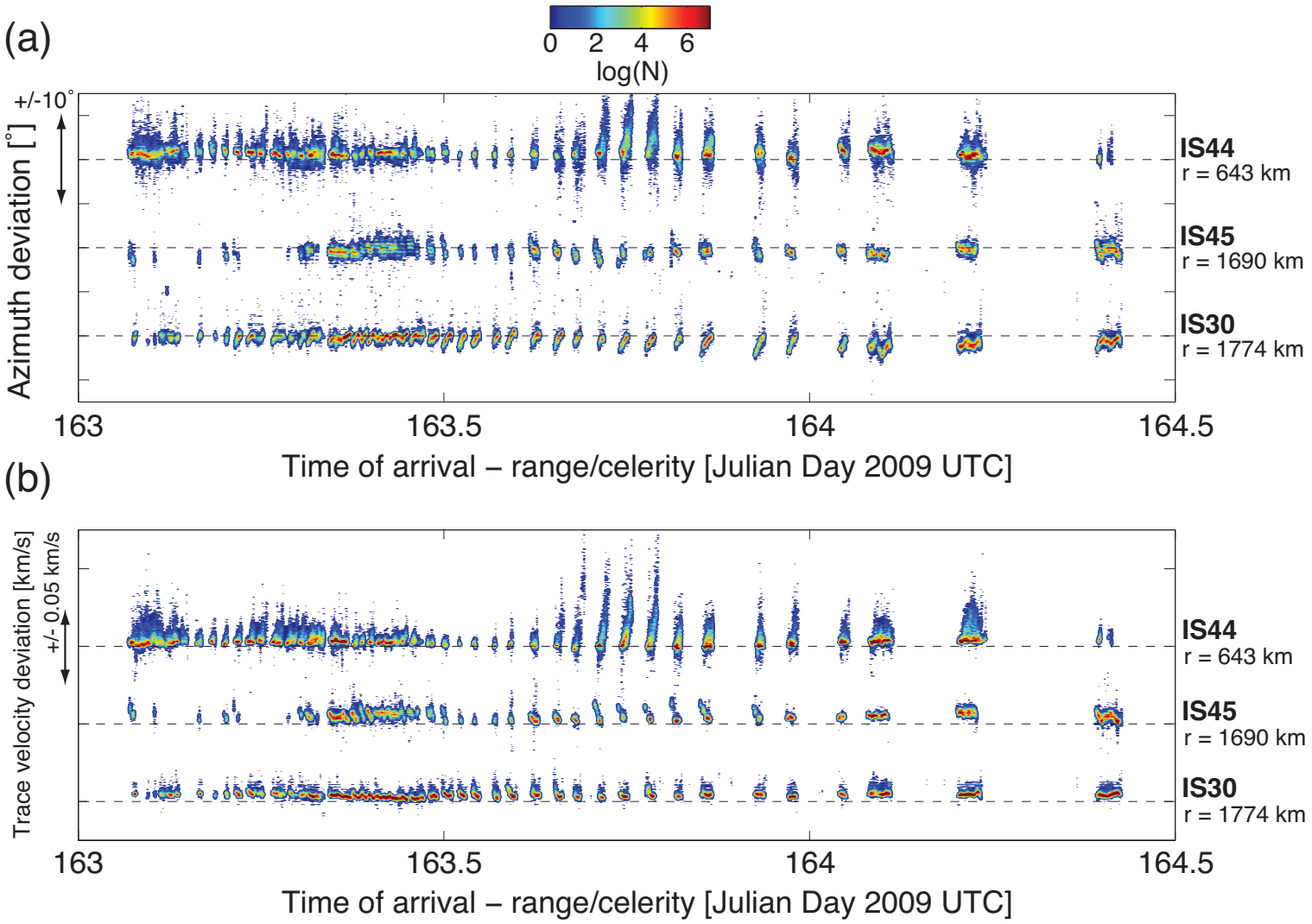

Figure 6
Click here to download Figure: figure_6.eps

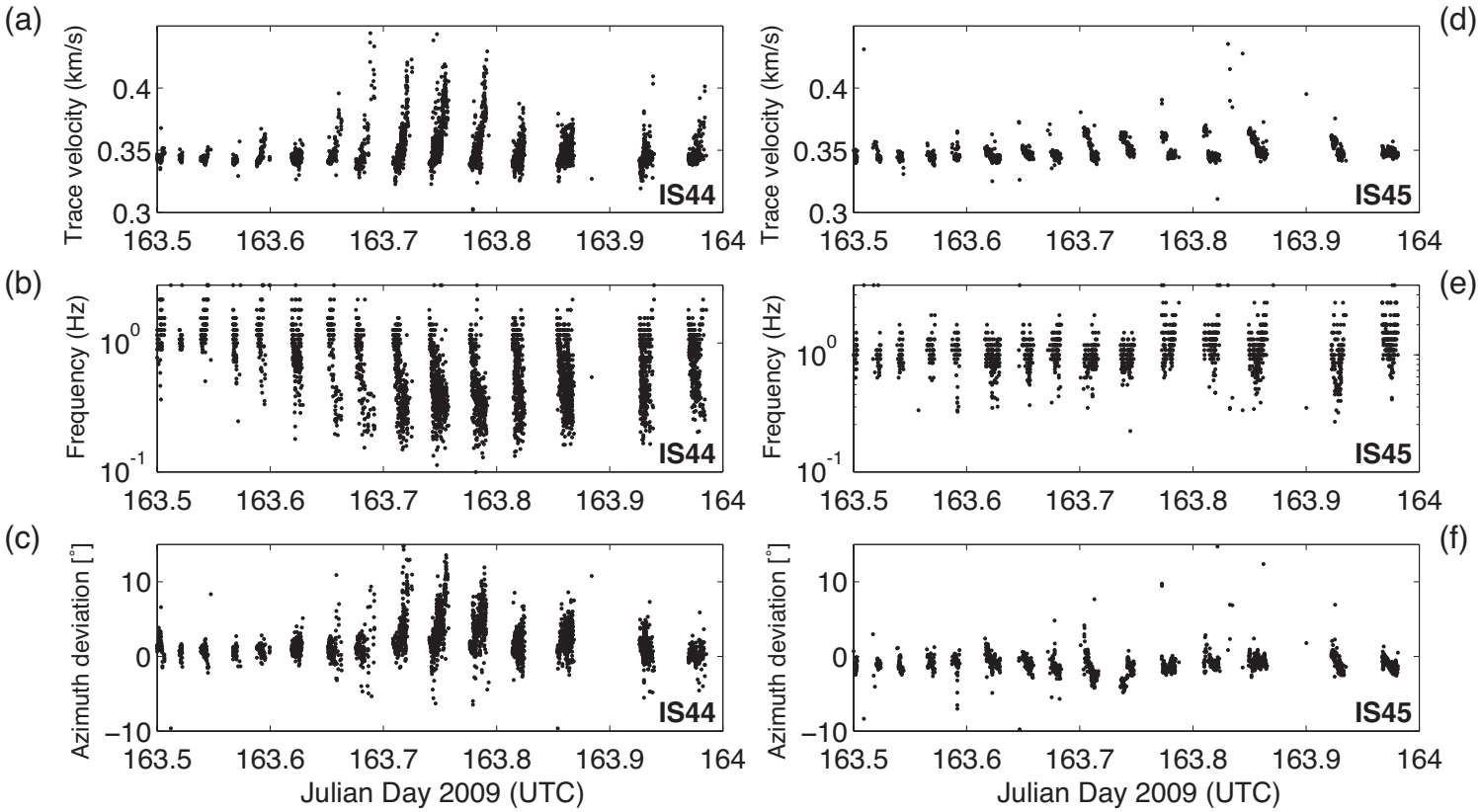

Figure 7

Click here to download Figure: figure_7.eps

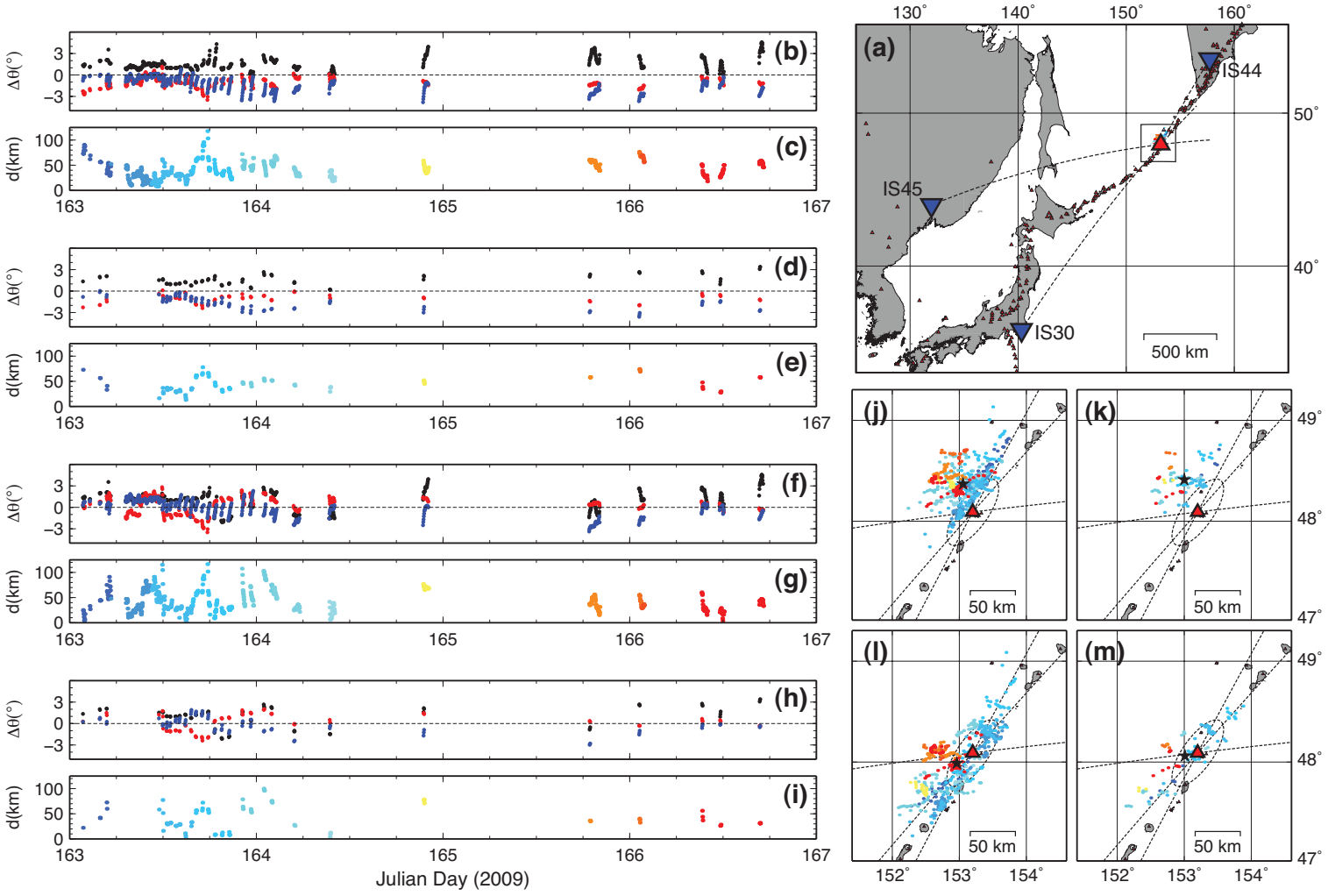

Figure 8
Click here to download Figure: figure_8.eps

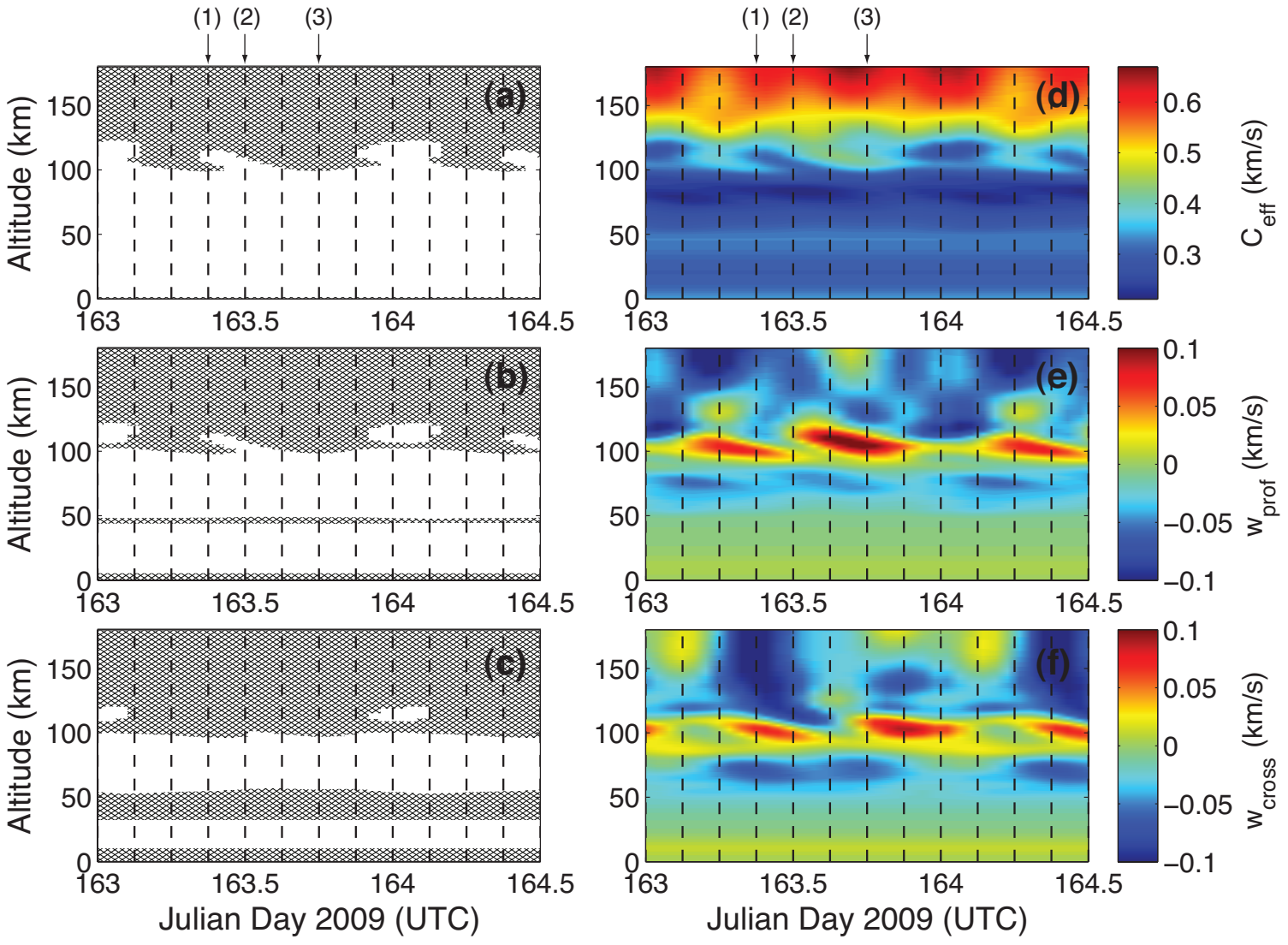

Figure 9

Click here to download Figure: figure_9.pdf

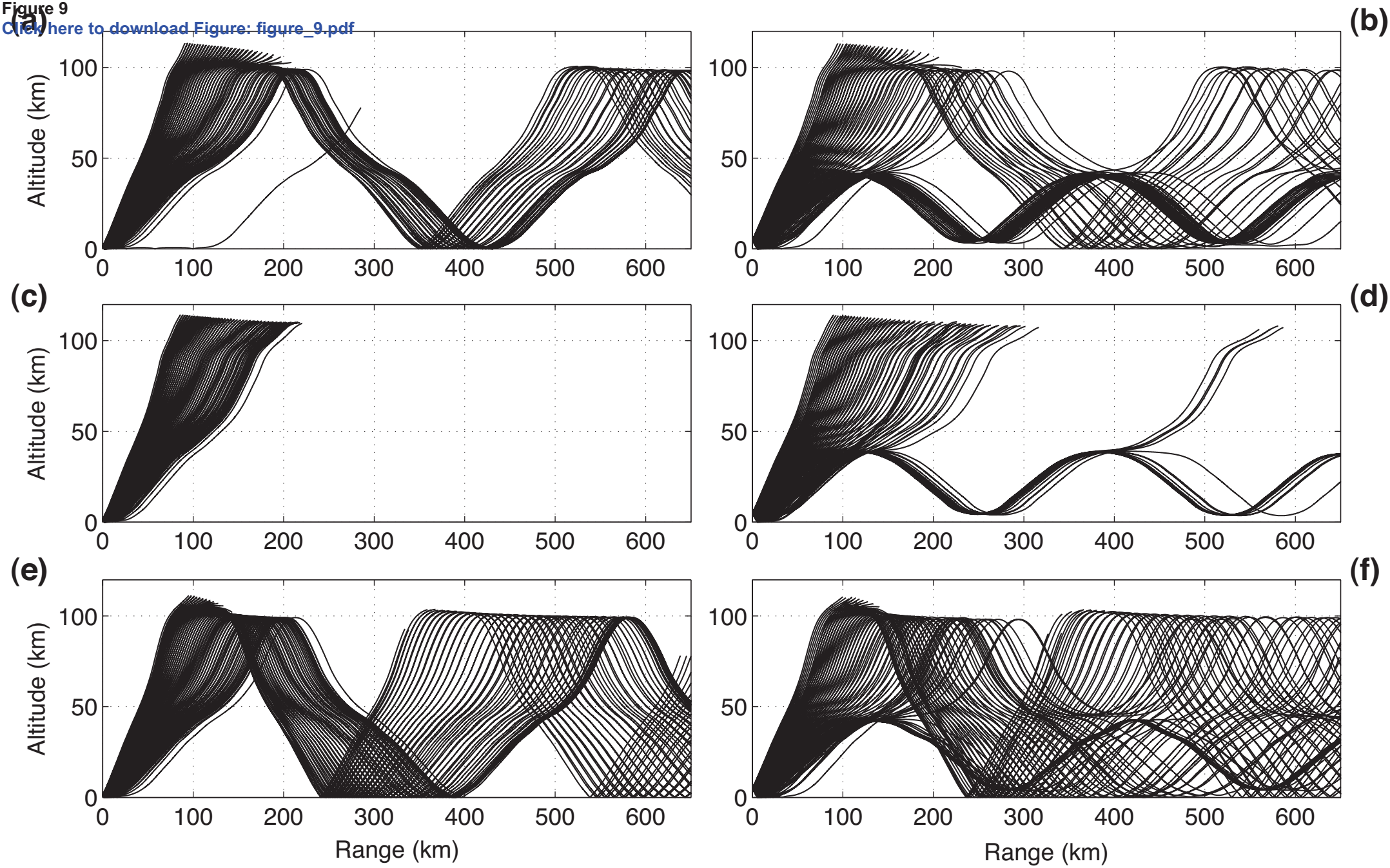

Figure 10
Click here to download Figure: figure_10.eps

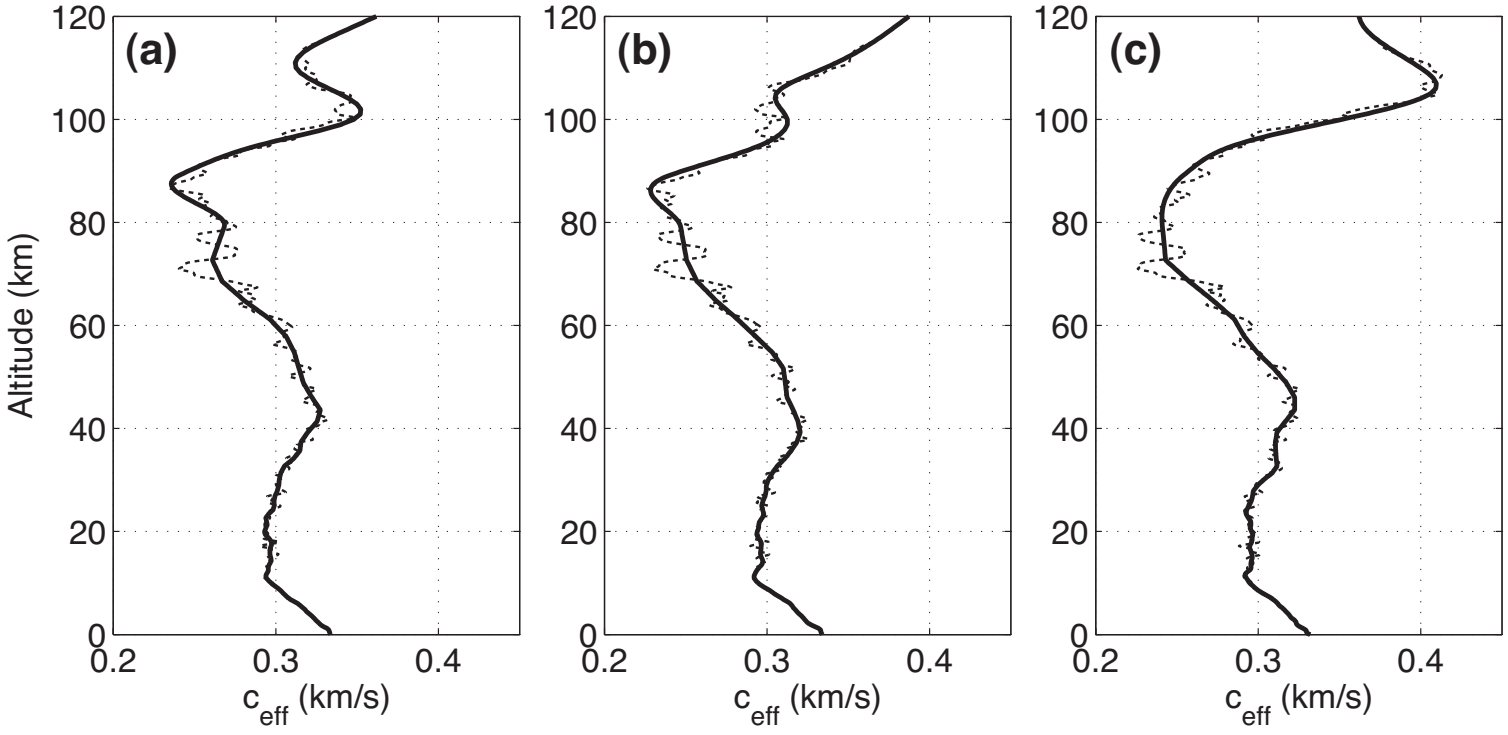

Figure 11
Click here to download Figure: figure_11.eps